

Mass Continuity Constraints on Ice Ablation in Greenland

A Thesis

Presented in Partial Fulfillment of the Requirements for the

Degree of Master of Science

with a

Major in Geology

in the

College of Graduate Studies

University of Idaho

by

Dakota R. Pyles

Approved by:

Major Professor: Timothy C. Bartholomaus, Ph.D.

Committee Members: Ginny A. Catania, Ph.D.; Felix H. Liao, Ph.D.; Elowyn M. Yager, Ph.D.

Department Administrator: Alistair MS. Smith, Ph.D.

August 2022

Abstract

Mass loss across the Greenland Ice Sheet (GrIS) margin is increasing, with dynamic ice flux into the oceans and negative surface mass balance (SMB) being the two main mechanisms of mass loss. In this study, we focus on the SMB component, particularly negative SMB changes in the marginal ablation zone. Currently, SMB models struggle to represent spatial and temporal ablation variations near the GrIS margin, and recent studies have recommended using in-situ measurements and new remote sensing datasets to improve model skill along the ice sheet boundary. We detail and demonstrate a new satellite-based mass budget approach for estimating ablation rates throughout the Upernavik Isstrøm (UI) and Kangiata Nunaata Sermia (KNS) outlet regions. From 2019-2021, we report 396 total ablation rates and uncertainties over nine seasonal, temperate periods, with average measurements of -2.13 ± 3.59 cm/d at UI and -2.50 ± 3.25 cm/d at KNS. Validation efforts using nearby Automatic Weather Station (AWS) observations from the Programme for Monitoring of the Greenland Ice Sheet (PROMICE) network are encouraging, as the ablation rates are within or closely reflect spatially bounded ablation observations. Our mass budget method also shows an ability to reproduce observed ablation rates ranging from ~ 0 to -6 cm/d. While the average uncertainty at UI and KNS is about ± 3.4 cm/d, uncertainty analysis reveals ablation rates at slow-flowing areas, with low longitudinal and transverse stresses, can be estimated within ± 2 cm/d. Further validation and uncertainty analyses may improve spatial confidence to where our method can be scaled across a considerable extent of the GrIS margin, without an AWS.

Acknowledgements

Before my time at the University of Idaho, I was fortunate and incredibly grateful to receive support from two awesome faculty members at the University of Montana, where I completed my undergraduate degree. I would like to acknowledge Dr. Marc S. Hendrix for his guidance as I prepared for graduate school, and his recommendation of me to an old friend and mentor, Dr. Donald Winston II. I worked closely with Dr. Winston as a field assistant in the western Montana Rockies. His passionate energy was a joy to be around. Dr. Winston passed away peacefully in March 2022, aged 90; may you rest in peace, Don.

To my committee members, Dr. Ginny A. Catania from the University of Texas at Austin, Dr. Felix H. Liao and Dr. Elowyn M. Yager from the University of Idaho. Thank you for your support throughout the research process, your questions and feedback helped guide this project in the right direction.

To my advisor, Dr. Timothy C. Bartholomaus, thank you for bringing me into your glacier dynamics lab at the University of Idaho. I appreciate your patience and encouraging words as I was learning to write code and developing the project early on. Thank you for inviting me to help with the Turner Glacier project in Alaska; that was an unbelievable experience that I will never forget, I am truly blessed for the opportunity. It was a pleasure to work with you over the past two years, your guidance throughout the project was invaluable. Thank you for everything.

Lastly, I would like to thank NASA for funding this work, by way of the “Understanding the Evolving Geometry of Outlet Glaciers in Greenland” grant (80NSSC18K1477), awarded to Dr. Timothy C. Bartholomaus and Dr. Ginny A. Catania.

Dedication

All my love, to all my people.

Table of Contents

Abstract	ii
Acknowledgments	iii
Dedication	iv
Table of Contents	v
List of Tables	vii
List of Figures	viii
Section 1: Introduction	1
Section 2: Background	4
2.1 Datasets	4
2.1.1 ATLAS/ICESat-2 L3A Land Ice Height	4
2.1.2 MEaSURES Greenland Ice Velocity	5
2.1.3 IceBridge BedMachine Greenland	5
2.1.4 PROMICE Automatic Weather Stations	6
2.2 Study Sites	6
2.2.1 Upernavik Isstrøm (UI)	7
2.2.2 Kangiata Nunaata Sermia (KNS)	8
Section 3: Methods	9
3.1 Ablation Equation	9
3.2 Ablation Geometry and Grids	10
3.3 Ice Thickness Change Rate	11
3.4 Vector Velocities	12
3.5 Velocity Gradients	16
3.6 Ice Thickness and Gradients	18
3.7 Depth-Averaged Terms and Circle Filtering	18

3.8 AWS Validation	18
Section 4: Results	20
4.1 Upernavik Isstrøm	21
4.2 Kangiata Nunaata Sermia	22
4.3 Validation with AWS Observations	25
Section 5: Discussion	27
Section 6: Conclusions	35
Section 7: References	36

List of Tables

Table 2.1 AWS temperature, radiative fluxes, and physical conditions.....	8
Table 4.1 General ablation results at Upernavik Isstrøm and Kangiata Nunaata Sermia.....	20
Table 4.2 Specific ablation results at Upernavik Isstrøm.....	21
Table 4.3 Specific ablation results at Kangiata Nunaata Sermia.....	23
Table 5.1 Average term value for low, moderate, and high uncertainties.....	32

List of Figures

Figure 2.1 Study site location map.....	7
Figure 3.1 Ablation grid and thickness change rate processing	12
Figure 3.2 Large- and small-scale velocity reconstruction	14
Figure 3.3 Circle sampling and finite difference schematics, and final circle-velocity derivation	17
Figure 3.4 AWS installation at Upernavik Isstrøm and pressure transducer assembly.....	19
Figure 4.1 Spatial distribution of ablation rates and uncertainties at Upernavik Isstrøm.....	22
Figure 4.2 Spatial distribution of ablation rates and uncertainties at Kangiata Nunaata Sermia	24
Figure 4.3 Mass continuity ablation rates compared to AWS observations.....	25
Figure 5.1 Sensitivity coefficients for all uncertainty equation terms.....	30
Figure 5.2 Average uncertainty change after individual term adjustment	31

1. Introduction

Since the 1990s, the GrIS has been losing mass at an accelerated rate due to a warming climate (Mouginot et al., 2019; Rignot and Kanagaratnam, 2006; van den Broeke et al., 2009), causing concerns about future sea level rise and prompting rigorous sea level projections (IPCC, 2014; Shepherd et al., 2012). Greenland's mass balance is driven by SMB changes and dynamic ice discharge via marine-terminating glaciers, which have caused 10.8 ± 0.9 mm of mean global sea level rise from 1992-2018 (The IMBIE Team, 2020). The GrIS stores ~ 7.4 meters water equivalent of mean global sea level (Morlighem et al., 2017), and currently, Greenland's contribution to sea level rise is growing faster than all other sources, making the ice sheet a major source of sea level rise (Rietbroek et al., 2016; van den Broeke et al., 2016). This increasing rate of sea level contribution is due to the GrIS's unstable response to the warming climate and its feedbacks, which may initiate irreversible mass loss on regional scales (Hanna et al., 2020). While surface mass balance (SMB) and dynamic ice discharge have contributed nearly equally to Greenland's total mass loss from 1992-2018 (The IMBIE Team, 2020), increased surface melting and runoff are emerging as Greenland's leading mass loss terms in the 21st century (Enderlin et al., 2014). If negative SMB changes remain the dominant sea level rise contributor, improving the performance of SMB models, particularly around the GrIS margins where SMB models have the greatest deficiencies (Fettweis et al., 2020), will be important for future mass balance and sea level projections. We present a method for quantifying SMB changes in the ablation zone, using the 2-D mass continuity equation, which evaluates mass change through ice thickness changes and ice flow mechanisms.

Ice sheet flow is controlled by two fundamental processes; (1) ice kinematics, which describe how the ice sheet responds to surface mass changes, irrespective of forces, and (2) ice dynamics, which consider the forces and stresses acting on a body of ice, as well as the rheological properties of the ice. More precisely, ice kinematics define how the ice sheet should flow based on the surface slope set by accumulation and ablation, with surface melt and runoff being the main physical mechanism of motion (Catania et al., 2020). Accumulation is dominated by snowfall, but other processes such as wind-blown snow, melt refreezing, avalanche deposition and frost/rime formation may contribute to accumulation (Cuffey and Paterson, 2010). Ablation occurs in several ways, most notably through meltwater runoff, surface and frontal melting, sublimation, and iceberg calving (Cuffey and Paterson, 2010). Ablation is forced by the energy budget's radiative and turbulent fluxes, including shortwave and longwave radiation, sensible heat, and latent heat. Shortwave radiation absorption has been identified as the most important energy source for seasonal melt cycles, however, in the low-lying ablation zone, the sensible and latent heat turbulent fluxes significantly affect

interannual melt variability (van den Broeke et al., 2011). The SMB anywhere on the ice sheet is defined as the difference between accumulation (mass gain) and ablation (mass loss) at the surface (Ettema et al., 2010). Applying SMB concepts to a glacier, if accumulation and ablation are equal, the glacier is balanced and in steady state; however, most glaciers are unbalanced, meaning that their size, shape, and mass will change over time. Ice dynamics are largely defined by stresses within a body of ice, which manifest through spatial changes in the ice velocity and thickness. Since ice is an incompressible material, when it's stressed, the ice will deform by stretching or compressing, depending on the orientation of the stresses; when stretched or compressed, the ice surface lowers or rises. To summarize, ice flows down a topographic gradient, where kinematic motion exists to offset SMB gradients and dynamic flow causes deformation, resulting in ice thinning or thickening.

Although kinematics and dynamics are exclusive descriptions of ice flow, when considered together, they describe how an ice body changes over time. This relationship is apparent in the 2-D mass continuity equation, where temporal ice thickness changes are controlled by the SMB and ice flux divergence:

$$\frac{\partial H}{\partial t} = \dot{b} - \nabla \cdot \vec{q} \quad (1)$$

In equation 1, $\frac{\partial H}{\partial t}$ is the rate of ice thickness change, \dot{b} is the SMB, and $\nabla \cdot \vec{q}$ is the ice flux divergence. The mass continuity equation states that ice thickness changes are the difference between the climate-controlled SMB and the dynamic ice flux divergence. However, in this study, we are interested in quantifying the SMB, particularly the ablation component; therefore, the continuity equation is rearranged to solve for SMB:

$$\dot{b} = \frac{\partial H}{\partial t} + \nabla \cdot \vec{q} \quad (2)$$

Through equation 2, a mass budget approach is used to estimate SMB changes at high spatial resolutions (1 km), near the GrIS margin. Mass budget methods require detailed knowledge of SMB and ice discharge on local scales, which has become possible with new and improved satellite data (Hanna et al., 2020). The recently launched ICESat-2 satellite (Markus et al., 2017) measures high resolution ice surface changes, InSAR derived velocity maps (Joughin et al., 2010) and a GrIS-wide ice thickness map (Morlighem et al., 2017) can quantify dynamic ice fluxes, and when all datasets are combined, SMB may be calculated. In addition, the continued operation and maintenance of the PROMICE AWS network (Fausto et al., 2021), largely located in low-lying marginal areas, facilitates validation efforts of SMB estimates. While the mass budget method has limited regional utility, one

major advantage is that mass balance is partitioned into SMB and dynamic discharge components, which can give insight into the physical processes driving mass change (Hanna et al., 2020; van den Broeke et al., 2016).

Large SMB uncertainties (Fettweis et al., 2020; The IMBIE Team, 2020) are typically the greatest source of error in mass budget methods (Vernon et al., 2013). Since ice-sheet wide SMB cannot be directly measured, regional climate models (RCM) are often used to simulate SMB (Hanna et al., 2020). Intercomparison of these SMB models revealed significant regional and seasonal discrepancies, prompting recommendations to implement a common ice sheet mask in future SMB modelling efforts to reduce uncertainties (Vernon et al., 2013). Using this recommendation, the GrIS SMB model intercomparison project (GrSMBMIP; Fettweis et al., 2020) discovered the greatest spread between model uncertainties were near the GrIS margins, in the ablation zone. Their results highlight SMB models' inability to accurately represent physical ablation processes, while stressing model improvements by integrating satellite data and in-situ measurements. A major deficiency in near-margin model performance is the low, 50-100 km horizontal resolution of Earth System Models (climate forcing fields used in RCM inputs), which are too coarse to reliably simulate SMB changes (Hanna et al., 2020). Still, RCMs can produce SMB outputs up to 5 km native resolutions (e.g., RACMO, HIRHAM; Fettweis et al., 2020). Superimposed on the climate forcing issue is the statistical downscaling of native RCM outputs across the narrow fjords of marine-terminating glaciers. To resolve marginal SMB gradients, RCMs may be downscaled to 1 km resolution (Noël et al., 2016), however, downscaling can misrepresent surface processes, such as runoff (van den Broeke et al., 2016). Assessing RCM/SMB model performance is valuable because the outputs contain spatial and temporal errors and biases, potentially compromising their dependability (Vernon et al., 2013).

In this study, our goals are to demonstrate a new satellite-based mass budget method for estimating ablation, which has scalable potential across much of the GrIS ablation zone, to provide ablation estimates at two locations along the western GrIS margin, and to help resolve spatial and temporal SMB changes at low-elevation areas. The ability to accurately estimate marginal SMB is important for better understanding the ice sheet's long-term health (Vernon et al., 2013), and its potential future contributions to sea-level rise. Past mass balance studies (Hanna et al., 2005; Rignot et al., 2008; Shepherd et al., 2012; van den Broeke et al., 2009) must rely upon SMB models and their uncertainties, which may impact the precision of the total mass balance estimates. Erroneous model outputs and mass balance estimates have major implications, especially in a warming Greenland climate, as these products are often used to project global sea level rise (Shepherd et al., 2012; The IMBIE Team, 2020) .

2. Background

2.1 Datasets

2.1.1 ATLAS/ICESat-2 L3A Land Ice Height

Surface elevation profiles are selected from NASA's ICESat-2 mission. Launched in September 2018, ICESat-2 is a satellite equipped with the state-of-the-art Advanced Topographic Laser Altimeter System (ATLAS) instrument designed to measure the Earth's surface with unprecedented detail. ICESat-2 builds upon NASA's original ICESat mission (2003-2009), greatly improving on the original design and technical specifications (Markus et al., 2017; Smith et al., 2019). The ATLAS instrument houses a laser altimeter split into six beams and organized into three beam pairs; the beam pairs are spaced by ~ 3.3 km, while two beams composing a pair are separated by ~ 90 meters (Markus et al., 2017). The 3x2 beam array, therefore, provides consistent and thorough spatial coverage of surface elevations across the GrIS. Further, ICESat-2 operates on quarterly 91-day repeat cycles, allowing for high-resolution seasonal surface measurements, which are critical for estimating ablation during temperate months. Since the early 1990s, ice sheet and mass changes have been captured by radar and laser altimeters, though laser altimetry has two key advantages in that surface elevation measurements exhibit minimal subsurface scattering and are capable of precise measurements over steep sloping, near-terminus regions (Smith et al., 2020). These advantages contribute to ICESat-2's utility in measuring ice sheet, glacier, and mass changes.

Of ICESat-2's many data products, we use the Land Ice Height (ATL06) product for geolocated land-ice surface elevation measurements. Derived from the lower-level Global Geolocated Photon Data (ATL03) product, the ATL06 algorithm describes land-ice surfaces by fitting 40 m along-track segments to thousands of ATL03 photon elevation measurements and spacing segment centers by 20 meters. This process creates a 50% overlap between consecutive linear segments (Smith et al., 2019), therefore, the final ATL06 product has a 40 m spatial resolution, posted at 20 m intervals. Critical to our project design, ATL06 elevation measurements contain a quality flag with ratings of 0 or 1, where 0 indicates the highest quality and 1 indicates the lowest quality measurements (Smith et al., 2019). High quality measurements must meet all four criteria outlined in Smith et al. (2019), while flagged low-quality measurements fail to meet at least one of the four criteria. We found that flagged measurements are generally associated with fast-flowing ice that is crevassed. After testing, we found that inclusion of the flagged measurements did not significantly affect our surface elevation change estimates, instead, they greatly improved the quantity and spatial coverage of points available for elevation differencing. Therefore, we opted to use all ATL06

measurements within our study sites. Still, the posting of high/low quality data for a given ICESat-2 cycle may be affected by cloud and fog presence, heavily crevassed terrain, ATL03 photon surface location, and photon return flight path, with cloud coverage often being the most problematic. For this reason, criteria for ICESat-2 cycle selection was based on consecutive 91-day repeat tracks with complete spatial coverage throughout the study sites. Consecutive quarterly cycles are only considered to maintain a consistent surface elevation differencing period.

2.1.2 MEaSURES Greenland Ice Velocity

Surface velocity data are obtained from NASA's MEaSURES program, in particular, from the 'Selected Glacier Site' dataset. This dataset provides velocity estimates at 55 major glacier outlet regions (200+ marine-terminating glaciers), near the GrIS margins. The velocity data are produced using feature speckle tracking and conventional interferometry synthetic aperture radar (InSAR) techniques (Joughin et al., 2002; Joughin et al., 2010), with image pairs provided from the TerraSAR-X and TanDEM-X twin satellites. The velocity fields have a 100 m spatial resolution and varying temporal resolutions of 11, 22, or 33 days, on an 11-day repeat cycle; however, the majority of velocity fields we use are at 11-day resolution. At our study sites, we collect a subset of all available x/y vector velocity fields from 2019 to 2021, concurrent with ICESat-2's operation. Velocity error estimates typically range from ~1 to 15 m/yr and are not proportional to the vector magnitude, meaning the errors of fast and slow-flowing ice are generally similar.

2.1.3 IceBridge BedMachine Greenland

Ice thickness estimates are sampled from the BedMachine Greenland v4 dataset, which provides complete spatial coverage of ice thicknesses across the GrIS at 150 m resolution. The ice sheet wide map was adapted by combining ice thickness observations from radar sounders (HiCARS and PARIS) and Operation IceBridge flight missions, then applying several interpolation methods to infill data gaps; all thickness observations were obtained between 1993 and 2016 (Morlighem et al., 2017). Thicknesses near the GrIS margin were primarily developed using a mass conservation method, while the ice sheet interior was mapped with kriging and interpolation (Morlighem et al., 2017). To create mass conservation estimates, radar and airborne data were combined with high-resolution, InSAR derived surface velocities. Areas of fast flowing ice (> 50 m/yr) produced the highest quality and most trustworthy mass conservation estimates, due to relatively smaller vector errors (Morlighem et al., 2014b). Here, we sample ice thicknesses from the ablation zone, where the mass conservation method was applied. However, at small scales, some of our sampled thicknesses are inferred by interpolation, kriging, or from the Greenland Ice Mapping Project DEM (Howat et al.,

2014). Mass conservation derived thicknesses have a typical reported error of 36 meters, however, the error may exceed 100 meters in areas where thickness observations are limited (Morlighem et al., 2013). Across our study regions, the ice thicknesses have an average error of ~52 meters, or ~9% the average measured thickness.

2.1.4 PROMICE Automatic Weather Stations

Ice ablation validation data are provided by PROMICE AWSs near our study sites. Climatic monitoring of the GrIS dates back to the late 1970s, however, year-round observations were not available until the 1990s when the Greenland Climate Network installed several AWS, most of which were located in the accumulation zone (Fausto et al., 2021). Since few stations were monitoring the low-lying ablation zone, PROMICE was developed to help address this issue. Initiated in 2007, the PROMICE project aimed to improve the understanding of spatio-temporal variability in Greenland's climate by installing additional AWS, mostly in the underrepresented ablation zone where melting dominates the SMB (Fausto et al., 2021). Currently, the PROMICE AWS network has 25 operational instruments, which deliver daily, hourly, and monthly climatic data products. The AWSs have proven to be a valuable resource for assessing the quality of satellite-based observations, calibrating RCMs, and other numerical models that seek to refine SMB reconstructions (Fettweis et al., 2020; Noël et al., 2018; Van As et al., 2014a). To validate ablation estimates, we use an ice ablation time-series product that is derived from a pressure transducer assembly described in Fausto et al. (2021). Important to note, the PROMICE AWS use a naming convention with suffixes of 'U' and 'L', standing for upper and lower, respectively. The lower designated AWS are positioned near the GrIS margin, while the upper AWS is located higher in the ablation zone, near the equilibrium line altitude.

2.2 Study Sites

Our ablation estimates are made across general outlet regions, still, we refer to study sites by the major tidewater glacier within the region. As such, we create ablation estimates at Upernavik Isstrøm and Kangiata Nunaata Sermia (*Figure 2.1a*). These outlet regions, approximately 930 km apart, were selected to test the mass continuity ablation method under different climate and ice dynamics systems. In addition, both sites have outstanding ICESat-2, MEaSUREs, and PROMICE data availability and quality.

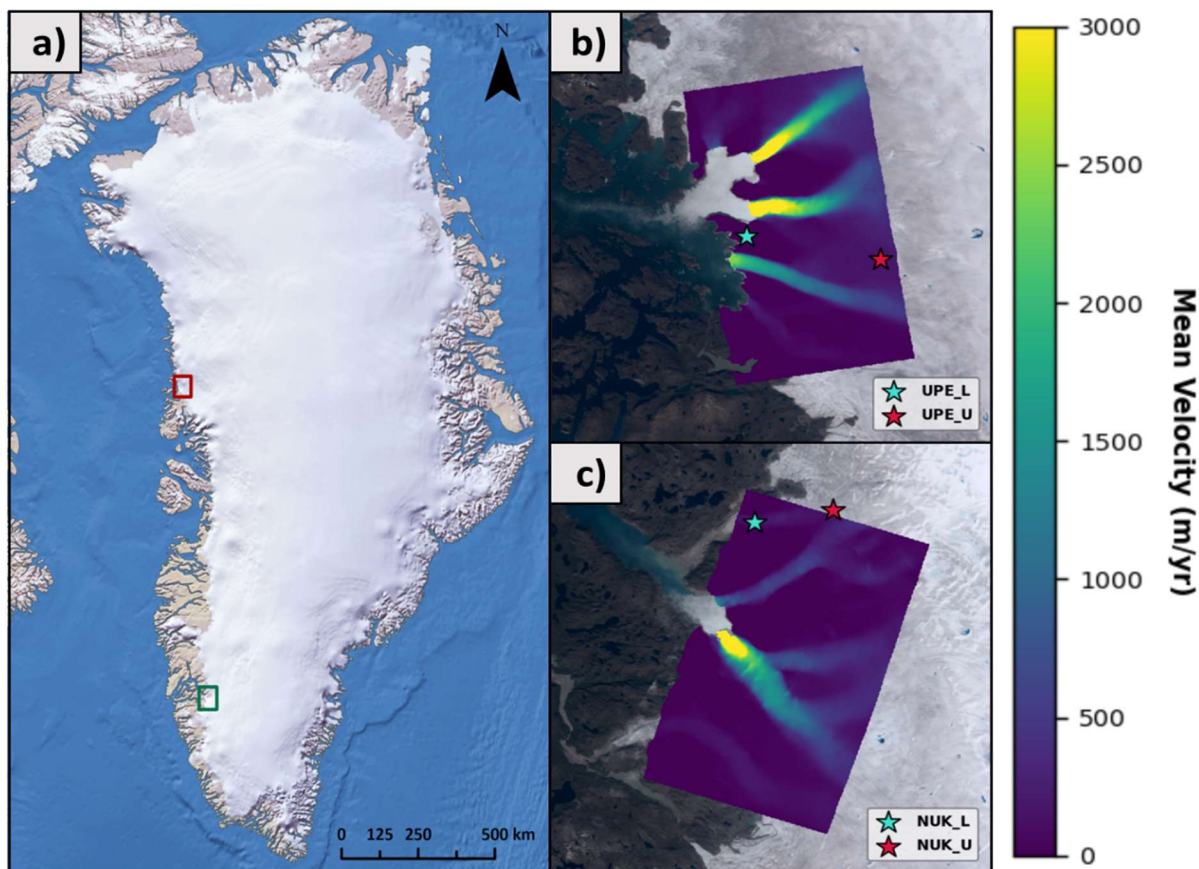


Figure 2.1: Study site location map. (a) Study site locations, relative to the GrIS; UI (red) lies on the west-central coast and is ~930 km north of KNS (green). (b) UI MEaSURES velocity grid (W72.90N) and AWS sites, plotted over an August 2019 Sentinel-2 optical image. All ablation estimates are created within the grid extent. The velocities represent the 3-year average velocity, on a cell-by-cell basis, for all velocity magnitude fields from 2019-2021. (c) Same as panel b, except at KNS (N64.25W).

2.2.1 Upernavik Isstrøm (UI)

Located in west-central Greenland ($72^{\circ}50'N$, $54^{\circ}10'W$), UI is characterized by a group of four tidewater glaciers that terminate into the Upernavik Icefjord (Larsen et al., 2016). Despite similar climate forcings, the four outlet glaciers exhibit asynchronous behavior, which may be explained by their distinct geometries (Larsen et al., 2016). Two PROMICE AWS (UPE_U and UPE_L) are situated within the MEaSURES velocity grid, which provide ablation observations that constrain much of the region (*Figure 2.1b*). From 2019-2021, UI has 33 available MEaSURES velocity fields: 14 in 2019, 10 in 2020, and 9 in 2021. In addition, five ICESat-2 repeat tracks (two flyovers spaced by 91 days) are available with consistent and complete spatial coverage throughout the MEaSURES grid, optimizing the number of potential ablation estimates; the five ICESat-2 cycles range from May 2019 to July 2021.

2.2.2 Kangiata Nunaata Sermia (KNS)

Flowing into the Nuup Kangerlua Fjord, KNS is the largest tidewater glacier in southwest Greenland (64°29'N, 49°61'W), draining ~2% of the GrIS (Moyer et al., 2017). While KNS is the largest, the region consists of three marine-terminating glaciers that also exhibit asynchronous behavior, however the causality is ambiguous (Motyka et al., 2017). Like UI, two PROMICE AWS are present at KNS (NUK_U and NUK_L), one of which is located within the MEaSUREs velocity grid, the other lying just outside the grid bounds (*Figure 2.1c*). These AWS are positioned closer to each other (~13 km), compared to the stations at UI (~23 km), therefore less area is constrained by KNS observations. KNS is generally warmer and receives slightly greater incoming radiative fluxes during temperate months (*Table 2.1*), therefore, we expect enhanced ablation rates across the region. At KNS, 35 MEaSUREs velocity fields are available from 2019-2021, distributed as follows: 14 in 2019, 11 in 2020, and 10 in 2021. There are four optimal ICESat-2 repeat flyovers, ranging from May 2019 to September 2020.

AWS Station	Air Temperature (°C)	Surface Temperature (°C)	Incoming SW Radiation (W/m ²)	Incoming LW Radiation (W/m ²)	Albedo	Elevation (m a.s.l.)
UPE_U	-3.10	-6.49 *	242 *	240 *	0.68	940
UPE_L	0.30	-2.86	213	271	0.65	220
NUK_U	-1.55	-11.24 **	245 **	250 **	0.78 *	1120
NUK_L	2.08	-1.64	216	276	0.41	530

* Limited Data; ** Mostly 2019 Data

Table 2.1: PROMICE AWS temperatures, incoming radiative fluxes, and physical conditions. Statistics are based on a 6-month, 3-year average from April to October, 2019-2021. The time period reflects the warmer seasonal climates at UI and KNS, and temporally bounds all ablation estimate periods. Sensible and latent heat turbulent fluxes are not included, due to poor temporal coverage. Given the temperature and elevation, greater ablation is expected at the lower designated ('L') AWSs. Similarly, more ablation is expected at KNS, given its southerly location.

3. Methods

3.1 Ablation Equation

To create remotely sensed ablation estimates, first we revisit the 2-D mass continuity equation to derive an ablation equation:

$$\dot{b} = \frac{\partial H}{\partial t} + \nabla \cdot \vec{q} \quad (2)$$

Recalling equation 2, the SMB term (\dot{b}) may be partitioned into its constitutive components, accumulation (c) and ablation (a):

$$c + a = \frac{\partial H}{\partial t} + \nabla \cdot \vec{q} \quad (3a)$$

In equation 3a, quantifying the accumulation term's contribution to ice thickness changes is difficult due to snow densification. When snow is on the ice surface, ICESat-2 surface elevation changes do not directly correspond to ice thickness changes. The mass continuity equation assumes that SMB rates and ice thickness changes have equal densities: the density of ice. Because of this assumption, snow densification is problematic, therefore, we constrain ablation estimates to mostly summer months when we assume accumulation equals zero. Thus, the accumulation term is dropped, and since we assume operation on bare ice, by definition, ICESat-2 surface elevation changes should directly correlate to ice thickness changes:

$$a = \frac{\partial H}{\partial t} + \nabla \cdot \vec{q} \quad (3b)$$

Here, negative ablation (a) values indicate mass loss and positive values signify mass gain. In the 2-D mass continuity equation, the ice flux divergence ($\nabla \cdot \vec{q}$) describes spatial ice flux changes in two dimensions, the ice flux in the x and y directions. Thus, the flux divergence in equation 3b may be split into exclusive x and y flux components, which transforms the flux divergence from a vector to a scalar field that defines the flux gradient:

$$a = \frac{\partial H}{\partial t} + \left(\frac{\partial q_x}{\partial x} + \frac{\partial q_y}{\partial y} \right) \quad (4a)$$

The ice flux is defined as the volume of ice flowing through a cross-section of a glacier over time. Ice fluxes are calculated from velocity and ice thickness measurements, such that $q_{x(y)} = uH$ (vH), where $q_{x(y)}$ is the ice flux, $u(v)$ is the x(y) depth-averaged velocity, and H is the ice thickness. The MEaSURES dataset provides surface velocity measurements, but we convert all surface-based

terms to depth-averaged terms before calculating an ablation rate (*see section 3.7*). The velocity and ice thickness products are substituted for ice flux in equation 4a, as follows:

$$a = \frac{\partial H}{\partial t} + \left(\frac{\partial}{\partial x} (uH) + \frac{\partial}{\partial y} (vH) \right) \quad (4b)$$

Through differentiation, by way of the product rule, the x and y flux components are expanded to reflect the dynamic relationships between ice velocity and thickness that impact temporal ice thickness changes:

$$a = \frac{\partial H}{\partial t} + \left(\left(u \frac{\partial H}{\partial x} + H \frac{\partial u}{\partial x} \right) + \left(v \frac{\partial H}{\partial y} + H \frac{\partial v}{\partial y} \right) \right) \quad (5)$$

Equation 5 is the final form of our ablation equation, where u is the x-vector velocity, v is the y-vector velocity, H is the ice thickness, $\frac{\partial u}{\partial x}$ and $\frac{\partial v}{\partial y}$ are velocity gradients in the x and y directions, $\frac{\partial H}{\partial x}$ and $\frac{\partial H}{\partial y}$ are the x and y ice thickness gradients, and $\frac{\partial H}{\partial t}$ is the rate of ice thickness change.

In addition, an ablation uncertainty is estimated by propagating the five ablation equation components in quadrature:

$$\Delta a = \sqrt{\Delta \left(\frac{\partial H}{\partial t} \right)^2 + \Delta \left(u \frac{\partial H}{\partial x} \right)^2 + \Delta \left(H \frac{\partial u}{\partial x} \right)^2 + \Delta \left(v \frac{\partial H}{\partial y} \right)^2 + \Delta \left(H \frac{\partial v}{\partial y} \right)^2} \quad (6)$$

In equation 6, the final four components are products, which require further expansion through the multiplication error propagation rule; the final uncertainty equation is as follows:

$$\Delta a = \sqrt{\left(\Delta \frac{\partial H}{\partial t} \right)^2 + \left(u \frac{\partial H}{\partial x} \sqrt{\left(\frac{\Delta u}{u} \right)^2 + \left(\frac{\Delta \frac{\partial H}{\partial x}}{\frac{\partial H}{\partial x}} \right)^2} \right)^2 + \left(H \frac{\partial u}{\partial x} \sqrt{\left(\frac{\Delta H}{H} \right)^2 + \left(\frac{\Delta \frac{\partial u}{\partial x}}{\frac{\partial u}{\partial x}} \right)^2} \right)^2 + \left(v \frac{\partial H}{\partial y} \sqrt{\left(\frac{\Delta v}{v} \right)^2 + \left(\frac{\Delta \frac{\partial H}{\partial y}}{\frac{\partial H}{\partial y}} \right)^2} \right)^2 + \left(H \frac{\partial v}{\partial y} \sqrt{\left(\frac{\Delta H}{H} \right)^2 + \left(\frac{\Delta \frac{\partial v}{\partial y}}{\frac{\partial v}{\partial y}} \right)^2} \right)^2} \quad (7)$$

3.2 Ablation Geometry and Grids

Before quantifying ablation estimates and uncertainties, we define the extent and geometry of ablation estimates at UI and KNS. Since we use remotely sensed data, by nature, spatial and temporal overlaps between datasets are sparse. Although ICESat-2 has ice-sheet-wide spatial coverage, our ablation estimates are limited to the spatial extent of the MEaSURES velocity grids. We estimate ablation inside a circular geometry, with the ablation rate representing the entire circle. We create an evenly spaced grid of ablation circles that closely follows the flight path of subsetted ICESat-2

ground tracks (*Figure 3.1a*). To maximize the number of circles in a grid, we extend the grid beyond the horizontal bounds of ICESat-2's beams by 2 km in each direction. The diameter of all circles comprising the grid is a constant 1 km. This diameter was chosen for three reasons; (1) to reduce potential sampling biases inherent in a smaller circle, (2) to ensure that circles are not too large, so that an ablation estimate is representative of the entire area within a circle, and (3) to maintain consistent circle sizes throughout a grid. Ablation equation terms are calculated by sampling vector points or raster cells inside a circle. Below we outline how each term is processed from the original dataset.

3.3 Ice Thickness Change Rate

The rate of ice thickness change $\left(\frac{\partial H}{\partial t}\right)$ is derived from ICESat-2's ATL06 data product. ATL06 measures surface elevations over time, however, because we constrain our ablation estimates to temperate months, when we assume accumulation is zero, surface elevation changes should directly reflect ice thickness changes. While some subglacial processes contribute to ice surface and thickness changes, such as the vertical bed separation rate (Andrews et al., 2014) and basal melt rate (Karlsson et al., 2021), these processes are insignificant compared to the changes on the ice sheet surface (The IMBIE Team, 2020); therefore, we assume all ice thickness changes occur at the surface. Thickness changes are calculated by differencing ATL06 surface elevations, at all six beams, from consecutive 91-day repeat ICESat-2 cycles. Since ATL06 measurements are not posted at exact locations upon repeat cycles and any given cycle may have missing data, we interpolate and average surface elevations onto a common line segment for each beam. Points on these segments are spaced 20 meters, consistent with ICESat-2's spatial posting. Point values are determined by searching for surface measurements within ± 20 meters of each point; in cases where multiple measurements are identified, a mean is taken. Geospatial coordinates are then assigned to the spatially averaged points by using the original along-track coordinates as an interpolant. This line segment process allows direct comparison of surface elevations from 91-day repeat flyovers. Once processed, the line segments are differenced at each beam. A single thickness change rate is determined by sampling thickness change points from all beams within the vertical bounds of an ablation circle (*Figure 3.1b*). A median thickness change and x-position is taken at each beam, then, with these six points an ordinary least squares regression is performed to predict the thickness change at the centroid x-position of a circle (*Figure 3.1c*). Thickness change rates of circles located outside the ICESat-2 horizontal bounds are extrapolated based on the linear regression; for this reason, we choose to extend the circle grid just 2 km to avoid over-extrapolation. To determine an uncertainty, a 95% prediction

interval is applied to a circle's prediction point, based on the linear regression. The uncertainty is defined as half of the prediction interval.

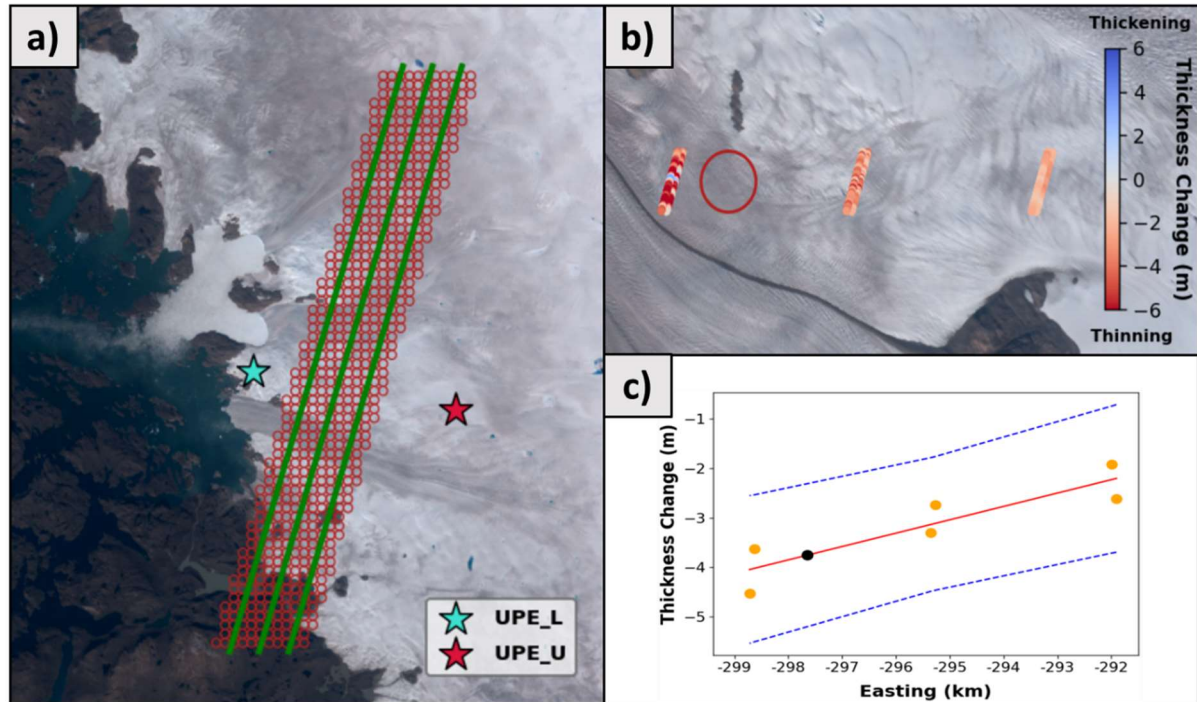


Figure 3.1: (a) An ablation circle grid (red circles) at UI mirroring the given ICESat-2 ground track (green lines). The grid is horizontally extended 2 km past the ICESat-2 extent to maximize potential ablation estimates. (b) On-ice image of thickness change (∂H) points within a circle's geometry. The median thickness change of all points is sampled at each beam; if the ICESat-2 spatial coverage is complete, a maximum of 50 thickness change points (per beam) may exist within the circle's vertical bounds. (c) The six median beam-sampled thickness changes (orange points) are used to linearly predict the thickness change at the circle center (black point). The blue dotted bars represent the 95% prediction interval, which defines the thickness change uncertainty.

3.4 Vector Velocities

MEASUREs velocity maps provide a basis for deriving the x-direction (u) and y-direction (v) velocities, however, we reconstruct, smooth, downscale, and daily interpolate these velocity fields to create a time-series consistent with our ICESat-2 periods. We apply these techniques because the original velocity maps have inconsistent spatial coverage, and less than ten maps are available around each summer. Empirical orthogonal functions (EOFs) are used to reconstruct spatial gaps in each of the 33 and 35 maps at UI and KNS, respectively. An EOF is derived by decomposing the signal of known data, if multiple coherent signals exist, then multiple EOFs may be defined. Each subsequently defined EOF is a mode that describes the spatial variance of the input data. As the data signal is decomposed, the modes become less coherent, and consequently, hold less weight in the reconstruction. Once all EOFs are defined, missing data are reconstructed by applying the appropriate

signal and weight of each EOF. In Earth science, EOFs are typically used in meteorology and oceanography, however, our EOF reconstruction reproduces acceptable velocity fields with plausible magnitudes and spatial patterns. To begin, we create a mean velocity map from 2019-2021, then calculate the velocity anomaly from the three-year mean for each map. An initial EOF reconstruction is performed, assuming the anomaly equals zero at unmeasured locations. From the initial reconstruction, the first four EOFs, which describe the prevailing spatial patterns in the velocity anomaly, are used to reconstruct the velocity anomalies. Only the first four EOFs are considered because additional EOFs have incoherent modes that explain less than 2% of the input data's spatial variance. During reconstruction, the anomaly maps are continuously updated until a sufficient solution is reached; the reconstruction is complete when the maximum difference between subsequent anomaly updates is less than 5 m/yr.

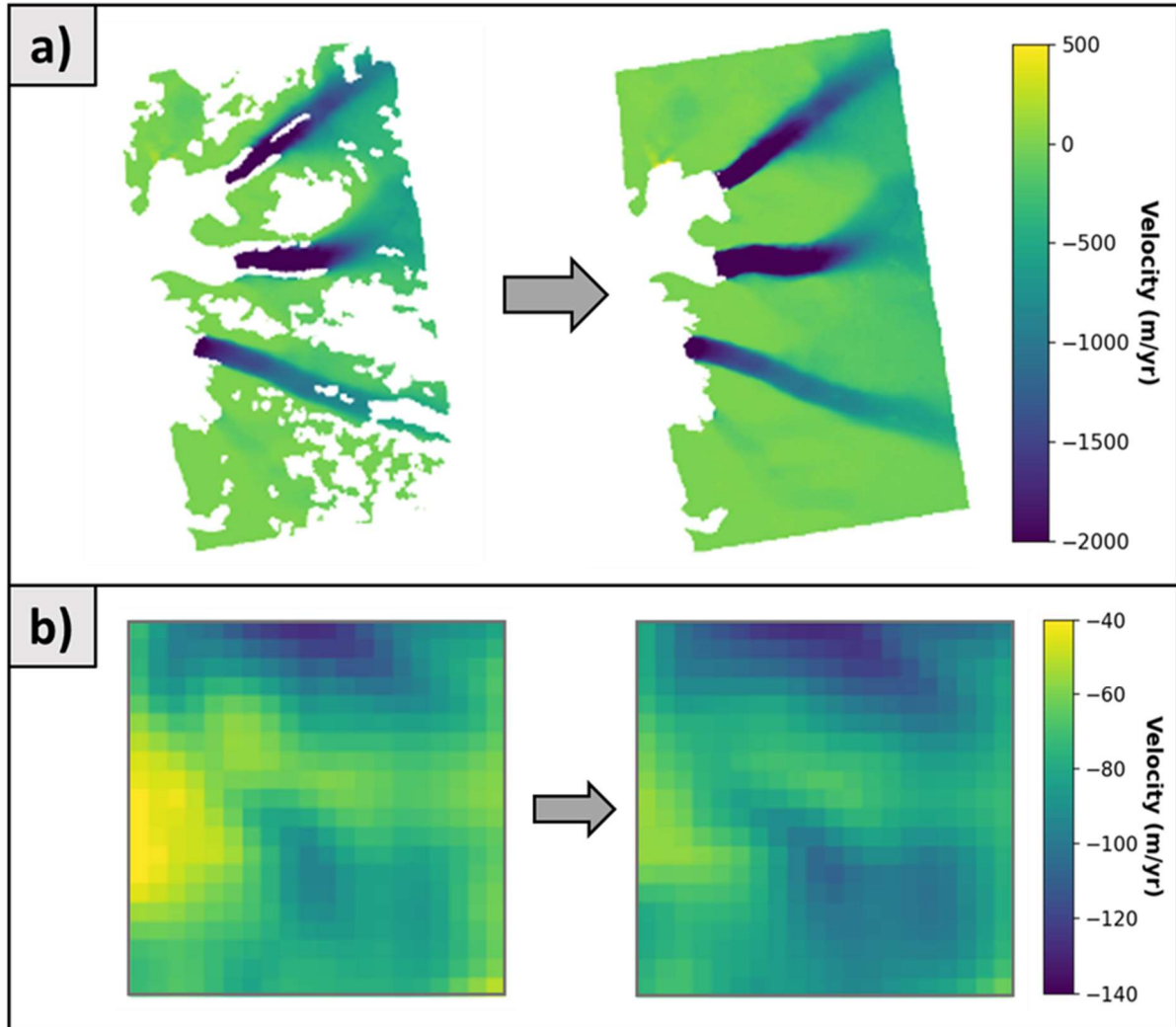


Figure 3.2: (a) Example of full velocity field reconstruction using EOFs. All x and y velocity fields at UI and KNS are reconstructed to their respective 2019-2021 mean spatial extent. (b) Small-scale (4 km^2) parcel comparison of original MEASUREs velocity to censored, reconstructed velocities at the same location. This comparison informs the reconstruction's typical contribution to the velocity error maps. The reconstruction reproduces original spatial velocity patterns with reasonable fidelity ($< 8\%$ average change) at UI and KNS.

After updating, the final anomaly maps are combined with the mean velocity map, resulting in velocity fields with complete spatial coverage (*Figure 3.2a*). To reduce noise, the reconstructed velocities are smoothed with a gaussian filter, using an $\sim 1200 \text{ m}$ kernel. The 100 m velocity fields are then downscaled to a 150 m resolution, matching the cell size of the BedMachine dataset; a cubic interpolation is used in the downscale. Finally, the median velocity of cells within a circle's geometry is sampled (*Figure 3.3a*). We sample median velocities for all maps bounding a 91-day ICESat-2 period, then linearly interpolate for each day between the sampled dates (*Figure 3.3c*). The median velocity of the 91 days composing an ICESat-2 period is taken as the circle's final vector velocity.

These velocity procedures are performed separately for x and y vector velocity maps, and the final median sampling is iterated for all circles within a grid.

Vector velocity uncertainties are difficult to assess, given the operations performed on the reported MEaSURES measurements, still, we account for each operation's contribution to the error with conservative thresholds. Since the velocities are reconstructed to the spatial extent of the 2019-2021 mean, missing errors must also be infilled to this extent. At UI and KNS, velocity errors do not scale with speed, instead the errors typically fall within a range of 1 to 15 m/yr. Thus, a constant absolute velocity is chosen to fill error gaps. The absolute velocity error is derived from a bivariate kernel density plot of all original MEaSURES velocity measurements and errors from 2019-2021. A conservative infilling value is manually selected for x and y velocities, based on the kernel density distribution; at UI (KNS), the x and y infilling errors are 7(5) and 9(7) m/yr, respectively. After filling missing error data with these velocities, we convert from absolute to relative errors, then propagate the relative errors and the effect of the EOF reconstruction in quadrature. Fittingly, the reconstruction's effect is only applied to infilled errors, where the measured velocity was reconstructed.

To quantify the reconstruction's contribution to the error, parcels where the original velocity is known are censored, then the EOF reconstruction is performed again. In this way, original velocity data can be directly compared to how the EOFs have recreated the data (*Figure 3.2b*). At UI and KNS, three 20 x 20 square parcels (4 km²) are masked from a selection of all available 2019-2021 velocity fields. If multiple velocity fields are available for a given year/month, then the first field for that year/month is masked. We use this criteria to not bias the reconstructed parcels to a particular time period, and to not oversample velocity fields for a given year/month, which may alter the EOFs spatial velocity patterns. In total, 10 of the 33 fields (12,000 cells) at UI, and 12 of the 35 fields (14,400 cells) at KNS are masked. Once reconstructed, the absolute value of the percent change from original to reconstructed data is calculated on a cell-by-cell basis for each field. Finally, the median of all magnitude-adjusted percent change measurements is taken as the reconstruction's impact. The reconstruction's impact at UI (KNS) for x and y velocities are ~5.6% (~3.8%) and ~7.6% (~5.9%), respectively.

To account for the gaussian smooth's error contribution, a percent change from original/reconstructed velocities to smoothed velocities is calculated on a cell-by-cell basis for each velocity field within or temporally bounding an ICESat-2 period. The percent changes are propagated in quadrature with the original and newly infilled/reconstructed relative errors, also on a cell-by-cell basis. The results are relative error maps, with complete spatial coverage, that account for the

reconstruction and smooth's effect, appropriately and conservatively. These relative error maps are then resampled to 150 m resolution and multiplied by the time-corresponding smoothed velocity field to convert back to absolute errors. From here, the absolute error maps follow the same median sampling and daily interpolation procedures as the vector velocities (*Figure 3.3c*). However, to account for the effect of time interpolation, the mean sampled velocity difference is propagated with the final 91-day median velocity error in quadrature. The mean sampled difference metric is determined by differencing consecutive median vector velocities of a circle, for all velocity fields within or bounding an ICESat-2 period. The mean velocity of these sampled differences is defined as the uncertainty for the daily interpolation, on a circle-by-circle basis. Thus, the mean sampled difference will reflect modest or substantial velocity variations in the sampled velocity fields for any given circle.

3.5 Velocity Gradients

The velocity gradients $\left(\frac{\partial u}{\partial x}, \frac{\partial v}{\partial y}\right)$ are calculated from the reconstructed, smoothed, and downsampled velocity fields. A second order finite difference is used to approximate the partial derivatives (*Figure 3.3b*); for example, the approximation's general form for $\frac{\partial u}{\partial x}$ is:

$$\frac{\partial u}{\partial x} \approx \frac{u(x + \Delta x) - u(x - \Delta x)}{2\Delta x}$$

Where $u(x + \Delta x)$ and $u(x - \Delta x)$ represent the velocities of cells adjacent to the approximated cell, and Δx is the raster spatial resolution, 150 meters. Complete finite difference maps are produced, then the median sampling and daily interpolation vector velocity methods are applied to obtain an x/y gradient value for each circle.

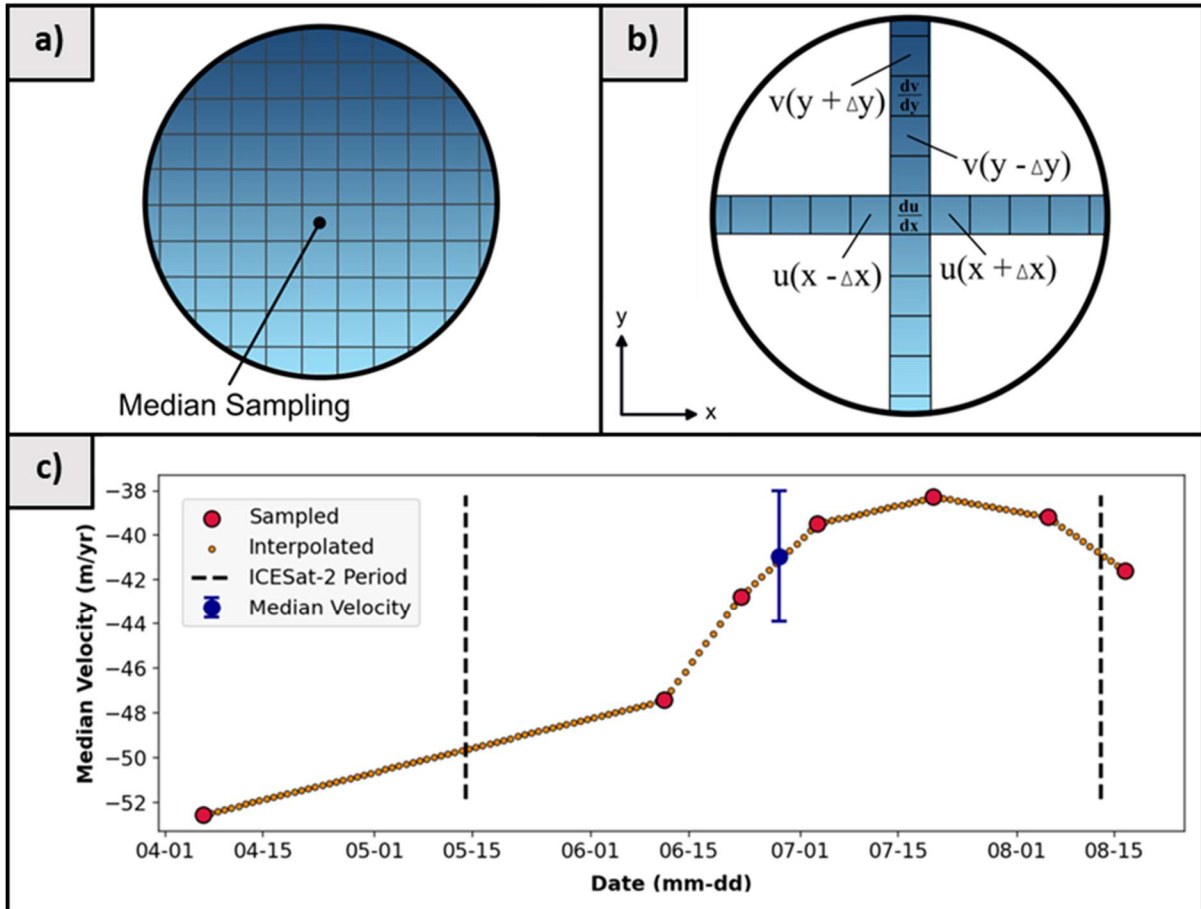


Figure 3.3: (a) Schematic for sampling the median velocity within circle geometry. (b) Schematic for finite difference approximations. Finite differences are calculated on a cell-by-cell basis, then a median is sampled as shown in panel a. (c) Example of daily interpolation and final median velocity sampling. Red points are the median circle-sampled velocities, and orange points are the linear, daily interpolated velocities. A final 91-day median velocity (dark blue point) is taken, corresponding to the given ICESat-2 period (black dotted lines). The error bars represent the mean sampled difference between all consecutive sampled points.

Velocity gradient uncertainties are produced by propagating the two velocity errors that correlate to the measurements used in a finite difference approximation. The velocity errors are sampled from the final vector velocity errors maps, and the errors are propagated in quadrature. Error propagation is performed everywhere a velocity gradient has been approximated, therefore, like the vector velocity error maps, there are complete gradient uncertainty maps. In addition, because velocity gradients are daily interpolated, we propagate the average sampled gradient difference onto the final 91-day averaged gradient error to account for the impact of time interpolation. Similar to the final vector velocities, the average sampled difference is propagated on a circle-by-circle basis, which reflects the variability of velocity gradients within each circle.

3.6 Ice Thickness and Gradients

The ice thickness (H) and gradients $\left(\frac{\partial H}{\partial x}, \frac{\partial H}{\partial y}\right)$ are determined with methods similar to the velocity terms. Since BedMachine is a time-averaged product, provided at a single time-step, daily interpolation is not necessary. However, we apply the previously described raster sampling and finite difference approximations to solve for all ice thickness terms. The only difference is that a mean, instead of median, is taken as the typical thickness and gradient value. A mean is used because outliers are rare, particularly in ice thicknesses derived from mass conservation, and the variance of thickness measurements within a circle is less extreme than velocity variations. The ice thickness uncertainty is the mean error within a circle, and like the velocity gradients, the thickness gradient uncertainties are the mean of propagated errors.

3.7 Depth-Averaged Terms and Circle Filtering

Once a measured and error value are obtained for each ablation equation term, the terms are converted to cm/d. Since all vector velocities and velocity gradients represent surface measurements, we transform these terms into more realistic depth-averaged measurements; the depth-averaged product is defined as 90% of the surface measurement, and to account for this adjustment, 10% of the surface measurement is propagated with the corresponding error in quadrature. Finally, an ablation estimate and uncertainty are calculated for all gridded circles, using equations 5 and 7. We report all ablation estimates with an uncertainty less than 5 cm/d, which generally reflect ideal criteria for producing lower uncertainty estimates.

3.8 AWS Validation

Ablation estimates are validated with a pressure transducer assembly, outfitted at each PROMICE AWS (*Figure 3.4*). The pressure transducer is placed at the bottom of a water/antifreeze filled hose, drilled over ten meters into the ice, and quantifies surface changes due to ice ablation by measuring the hydrostatic pressure of the vertical liquid column above the sensor (Fausto et al., 2021). After correcting for the influence of air pressure variations, reductions in hydrostatic pressure correlate directly to ice ablation (Fausto et al., 2021). More details about the transducer assembly and function are outlined in Fausto et al (2021). The observed AWS ablation is calculated as the difference between the water column depth on the first and last day of a given ICESat-2 period. Although there are five ICESat-2 periods at UI and four at KNS, as well as two AWS stations at each study site, we only compare ablation estimates within 2 km of an AWS; these areas are most likely to have physical conditions and ablation rates that are comparable to the AWS.

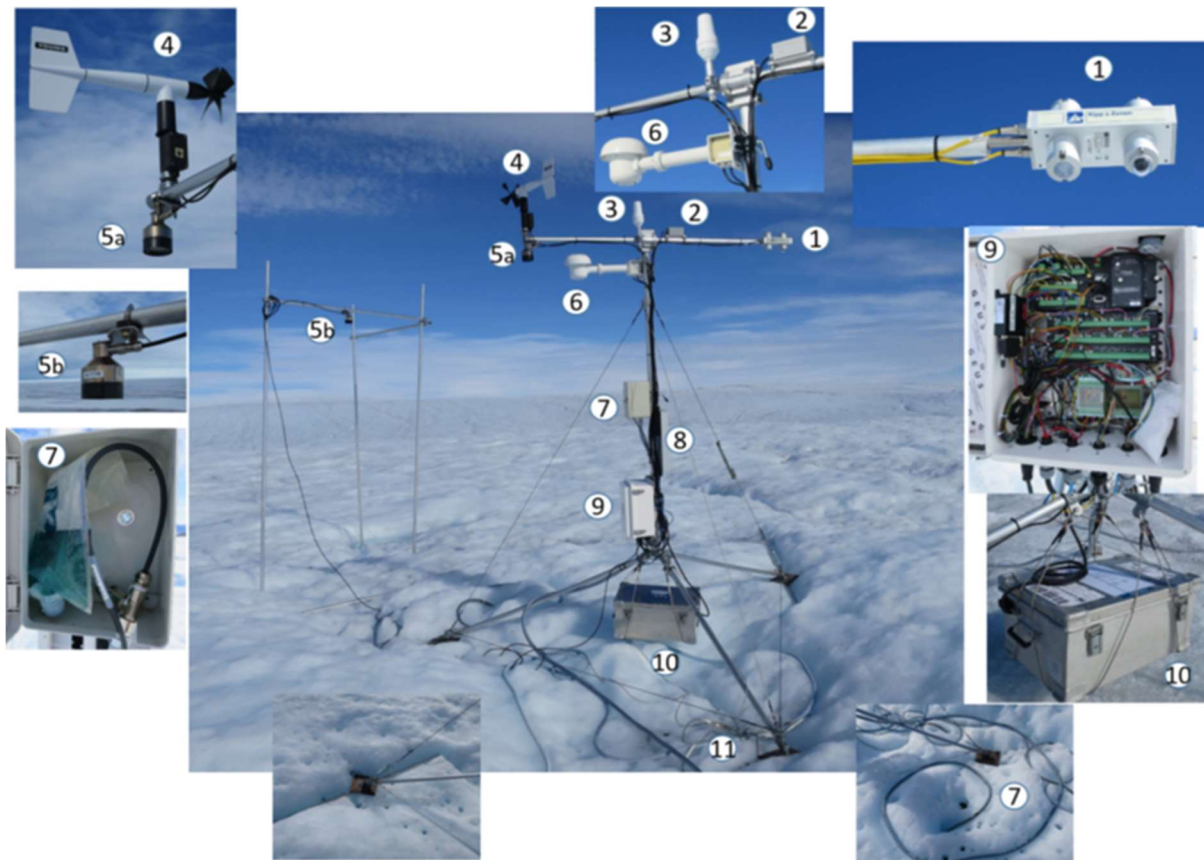


Figure 3.4: Photograph of the PROMICE AWS installation at UPE_U (Fausto et al., 2021). Objects labeled with a ‘7’ denote the pressure transducer assembly, which measures ice ablation directly and is used to validate our mass continuity ablation estimates.

4. Results

At UI and KNS, ablation rates are produced for five and four ICESat-2 periods, respectively. In total, we report 396 ablation rates with uncertainties less than ± 5 cm/d. Coincidentally, UI and KNS returned 198 estimates each, which is useful for a general outlet region comparison (*Table 4.1*), despite variable estimate quantities over different ICESat-2 periods.

Outlet Region	Total Estimates	Average Ablation (cm/d)	Average Uncertainty (\pm cm/d)	Average AWS 'U' Ablation (cm/d)	Average AWS 'L' Ablation (cm/d)
UI	198	-2.13	3.59	-1.70	-2.11
KNS	198	-2.50	3.25	-1.76	-3.85

Table 4.1: General ablation results at UI and KNS. The ablation and uncertainty rates are the mean of all estimates, over all ICESat-2 periods (2019-2021). Likewise, AWS ablation rates are averaged at the upper ('U') and lower ('L') stations for the same periods.

Averaged for all estimates across the entire outlet region, we report an ablation rate of -2.13 cm/d at UI and -2.50 cm/d at KNS. The average uncertainties suggest slightly lower confidence in the estimates at UI (± 3.59 cm/d), compared to KNS (± 3.25 cm/d). The ablation rate at KNS is within the upper and lower AWS bounds, whereas the ablation rate at UI slightly overestimates the lower AWS rate. However, the AWS observed rates at UI have a tighter spread (0.41 cm/d) than at KNS (2.09 cm/d), reducing the likelihood of producing a spatially bounded rate. Although, the ablation rate is overestimated at UI, the majority of ablation estimates are located closer to the lower AWS at both study sites, therefore the estimates at UI and KNS should be more representative of the lower AWS rate. However, the average KNS ablation rate is more comparable to the upper AWS rate. This is likely due to a significantly steeper ablation gradient at KNS; not only is the observed spread greater at KNS, but the AWSs are positioned closer (~ 13 km) than UI's (~ 23 km). Consequently, ablation rates at KNS have greater spatial variability and observed rates are more difficult to reproduce. Still, greater ablation rates are observed at the lower-lying AWSs, confirming the expected mass loss relationship with elevation and proximity to the margin. Also expected, our ablation rates and the AWS observations agree with enhanced ablation at the southerly KNS region. To provide complete context, we examine the ablation estimates from all ICESat-2 periods and their spatial distribution at each site.

4.1 Upernavik Isstrøm

At UI, ablation rates are consistently within the AWS observation bounds and are more comparable to closer UPE_L station (*Table 4.2*). The June to September 2020 period has a small sample size over faster-flowing ice and is not representative of the observed ablation; this period is not further considered but is analyzed in the discussion. The uncertainties are consistent across all ICESat-2 periods, suggesting temporal reliability in uncertainties across slow-flowing ice. The greatest observed rates in 2019 are reflected in our 2019 estimates, and similarly, we appropriately estimate the lower observed rates in 2020 and 2021. Perhaps, the mass continuity method can not only capture spatial ablation gradients, but can also distinguish annual ablation variability.

ICESat-2 Period	Total Estimates	Average Ablation (cm/d)	Average Uncertainty (\pm cm/d)	UPE_U Ablation (cm/d)	UPE_L Ablation (cm/d)
May 14 : Aug 13, 2019	67	-2.89	3.73	-3.27	-2.95
Jun 12 : Sep 11, 2019	19	-2.51	3.42	-3.25	-2.86
Apr 4 : Jul 4, 2020	13	-0.60	3.43	-0.26	-0.65
Jun 30 : Sep 29, 2020	2	-3.43	4.18	-0.79	-2.09
May 1 : Jul 31, 2021	97	-1.72	3.54	-0.94	-2.00

Table 4.2: Ablation results for all five ICESat-2 periods at UI. All ablation and uncertainty estimates are averaged for each period. AWS rates are the observed ice ablation over the respective ICESat-2 period.

Spatially, the ablation estimates are clustered around low-lying, slow-flowing ice (*Figure 4.1*). On small scales (2-5 km), coherent ablation patterns are evident, with the lowest rates and uncertainties typically situated on the slowest flowing ice. Ablation and uncertainty magnitudes become progressively larger towards the fast-flowing, marine-terminating glaciers. These spatial patterns highlight the mass continuity method's utility and weaknesses; mass continuity can distinguish ablation gradients at high resolutions, but struggles to estimate reasonable ablation rates with low uncertainties on the dynamic glacier trunks.

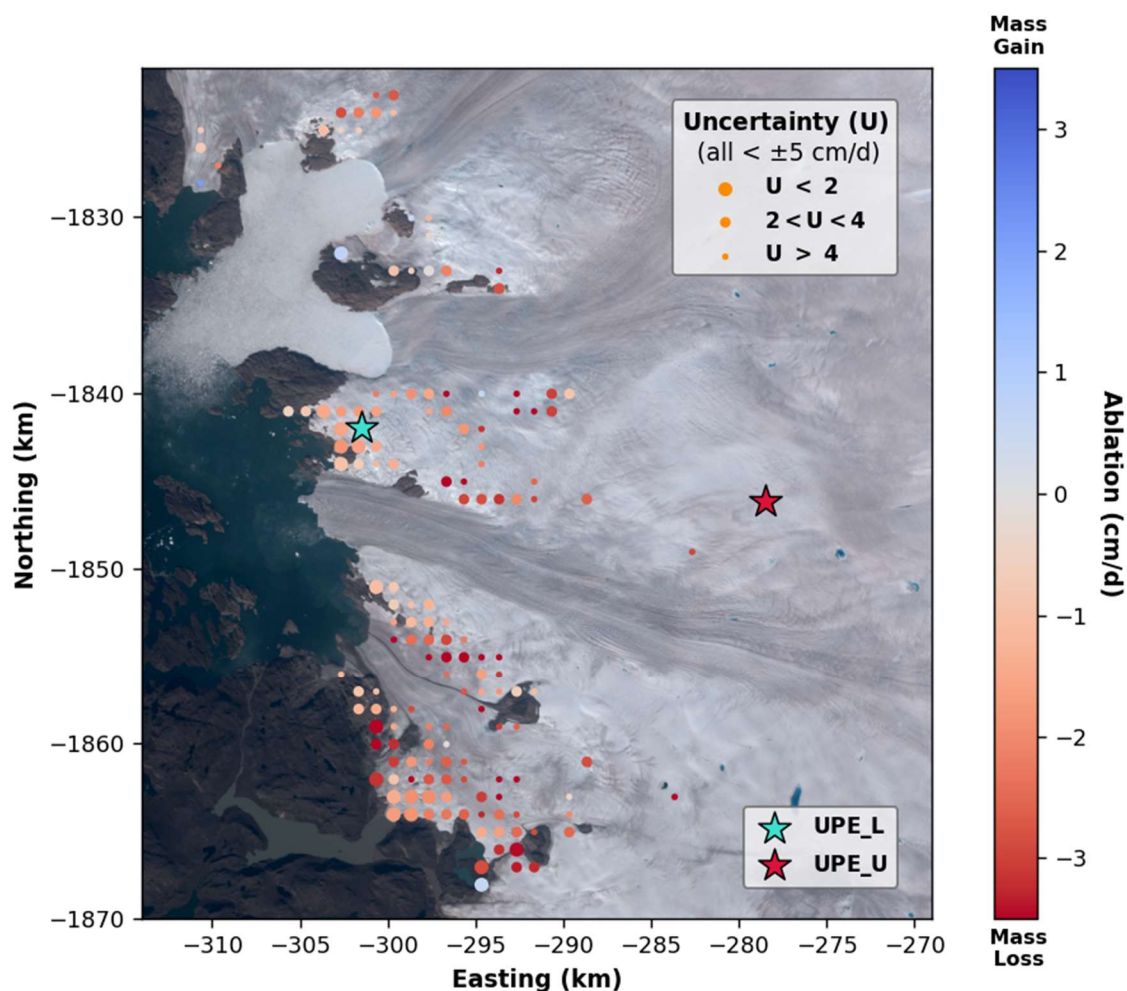


Figure 4.1: Composite spatial distribution of ablation rates and uncertainties, plotted over an August 2019 Sentinel-2 image at UI. All unique ablation circle geometries are shown, from all ICESat-2 periods at UI; if a circle geometry contains multiple estimates from separate periods, the lower uncertainty estimate is plotted. Reds indicate mass loss, blues indicate mass gain, and grey represents mass-balanced areas. All uncertainties are less than ± 5 cm/d and denoted by three circle sizes: large circles ($< \pm 2$ cm/d), medium circles (± 2 to 4 cm/d), and small circles ($> \pm 4$ cm/d). Stars are the AWS locations; UPE_L (turquoise) and UPE_U (red).

4.2 Kangiata Nunaata Sermia

Ablation rates at KNS do not agree as well with AWS observations, underestimating ablation during enhanced melting periods in 2019 and 2020 (*Table 4.3*). The average uncertainties are very consistent, more so than at UI, strengthening the idea of temporally reliable uncertainties. Like UI, the AWS observations reveal enhanced ablation in 2019, compared to 2020. Our greatest ablation rate (-2.97 cm/d) occurs in 2019 too and is aided by the largest sample size (110 estimates) of all ICESat-2 periods in the study. Warm AWS air temperatures from May to September 2019 at KNS (~ 0.8 to 4.3 °C) and UI (~ 0.8 to 4 °C), combined with enhanced ablation observations, suggest increased mass loss across the western GrIS in 2019.

ICESat-2 Period	Total Estimates	Average Ablation (cm/d)	Average Uncertainty (\pm cm/d)	NUK_U Ablation (cm/d)	NUK_L Ablation (cm/d)
May 27 : Aug 26, 2019	110	-2.97	3.25	-3.31	-5.58
Apr 2 : Jul 2, 2020	14	-0.37	3.26	-0.19	-2.01
May 24 : Aug 23, 2020	58	-2.35	3.24	-1.72	-4.35
Jul 2 : Sep 30, 2020	16	-1.77	3.22	-1.83	-3.44

Table 4.3: Ablation results for the four ICESat-2 periods at KNS. All ablation and uncertainty estimates are averaged for each period. AWS rates are the observed ice ablation over the respective ICESat-2 period.

A particularly powerful result is the sequential progression of AWS ablation rates between the three near-evenly spaced ICESat-2 periods in 2020. The NUK_L rate is low in spring (-2.01 cm/d), significantly increases in summer (-4.35 cm/d), and tapers to a medium by fall (-3.44 cm/d). Our ablation rates mirror this observed 2020 trend, with -0.37 cm/d during spring, -2.35 cm/d in summer, and -1.77 cm/d by fall. While only based on the temperate seasons of 2020, the mass continuity method shows an ability to capture intra-annual ablation variations.

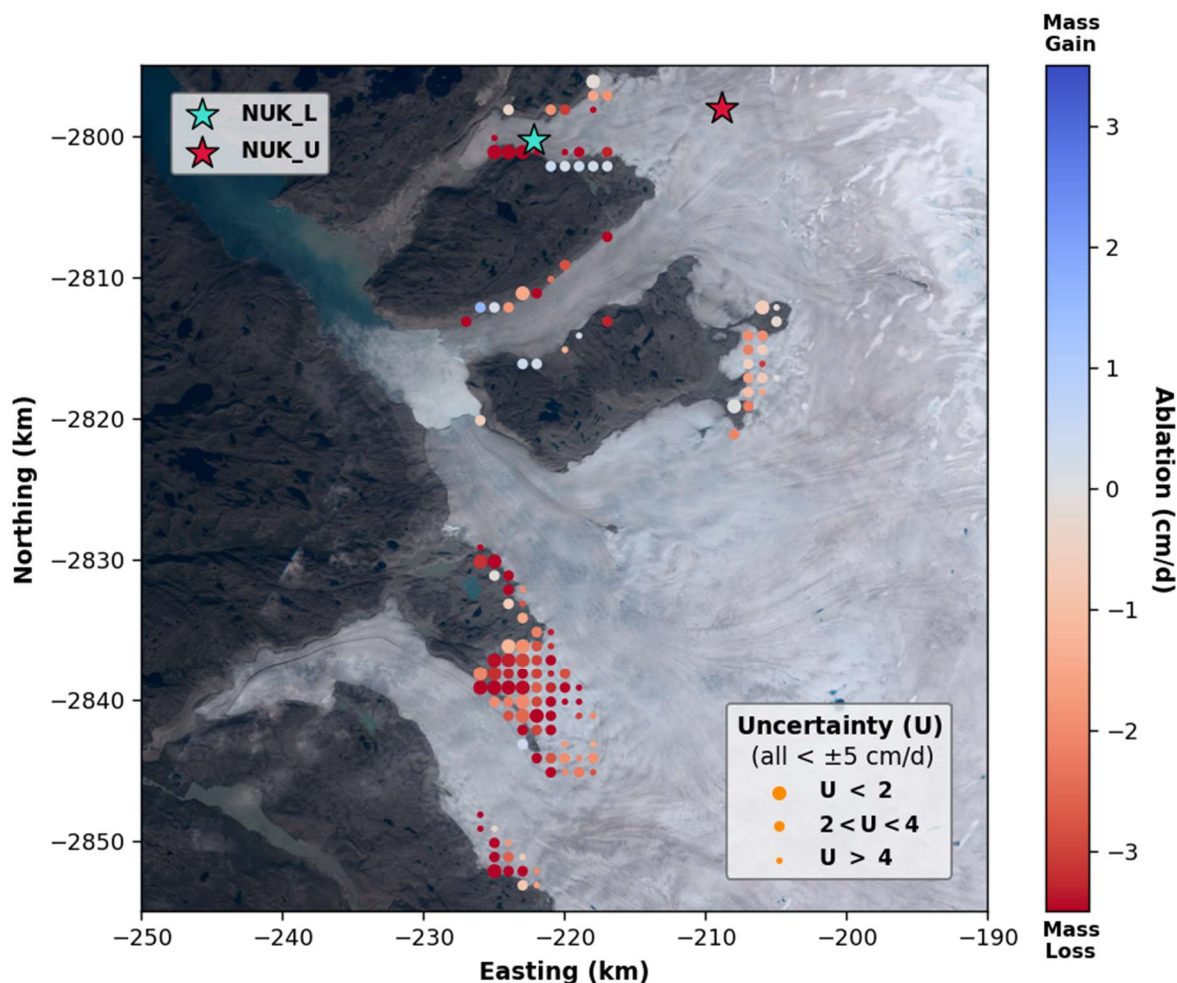


Figure 4.2: Composite spatial distribution of ablation rates and uncertainties, plotted over an August 2019 Sentinel-2 image at KNS. All unique ablation circle geometries are shown, from all ICESat-2 periods at KNS; if a circle geometry contains multiple estimates from separate periods, the lower uncertainty estimate is plotted. Reds indicate mass loss, blues indicate mass gain, and grey represents mass-balanced areas. All uncertainties are less than ± 5 cm/d and denoted by three circle sizes: large circles ($< \pm 2$ cm/d), medium circles (± 2 to 4 cm/d), and small circles ($> \pm 4$ cm/d). Stars are the AWS locations; NUK_L (turquoise) and NUK_U (red).

Similar to UI, ablation estimates are located on low-lying, slow-flowing ice, however, some estimates are reported along the boundaries of land- and marine-terminating glaciers (*Figure 4.2*). Ablation rates along the two north-most glacier margins provide circumstantial support of the mass continuity method's utility; south-facing slopes are characterized by greater ablation rates than the more shaded northern aspects. Some of these marginal glacier estimates indicate mass gain or balance, perhaps from avalanching or wind-blown snow deposition from the mountain slopes. In addition, ablation generally decreases further inland, an expected result that is observed by the AWSs. Like UI, proximal ablation estimates have coherent spatial patterns, which may indicate the prevailing behavior of localized surface processes.

4.3 Validation with AWS Observations

We attempt to validate the mass continuity method by comparing 11 ablation measurements with three AWS observations, from three distinct ICESat-2 periods (*Figure 4.3*). Two ablation rates correspond to the NUK_L observation from May 27 to August 26, 2019 (-5.58 cm/d), two rates at UPE_L from April 4 to July 4, 2020 (-0.65 cm/d), and seven rates at UPE_L from May 1 to July 31, 2021 (-2 cm/d); therefore, the three AWS rates represent distinct intra-annual periods, over three separate years, supporting temporal validation. All 11 ablation rate centroids are within 2 km of their respective AWS observation, which should closely resemble the observed rates and support spatial validation. The upper AWSs, NUK_U and UPE_U, are not considered as zero rates are within 2 km of the stations. Since ablation grids follow the ICESat-2 ground tracks, in most cases the gridded circles are not near an AWS, explaining why only 11 of 396 total estimates are available for validation. While the sample size is small, the mass continuity estimates compare reasonably to the AWS observations, with eight underestimations and three overestimations. All ablation rates are within ± 0.87 cm/d of their corresponding AWS observation, and ten rates are within ± 0.55 cm/d.

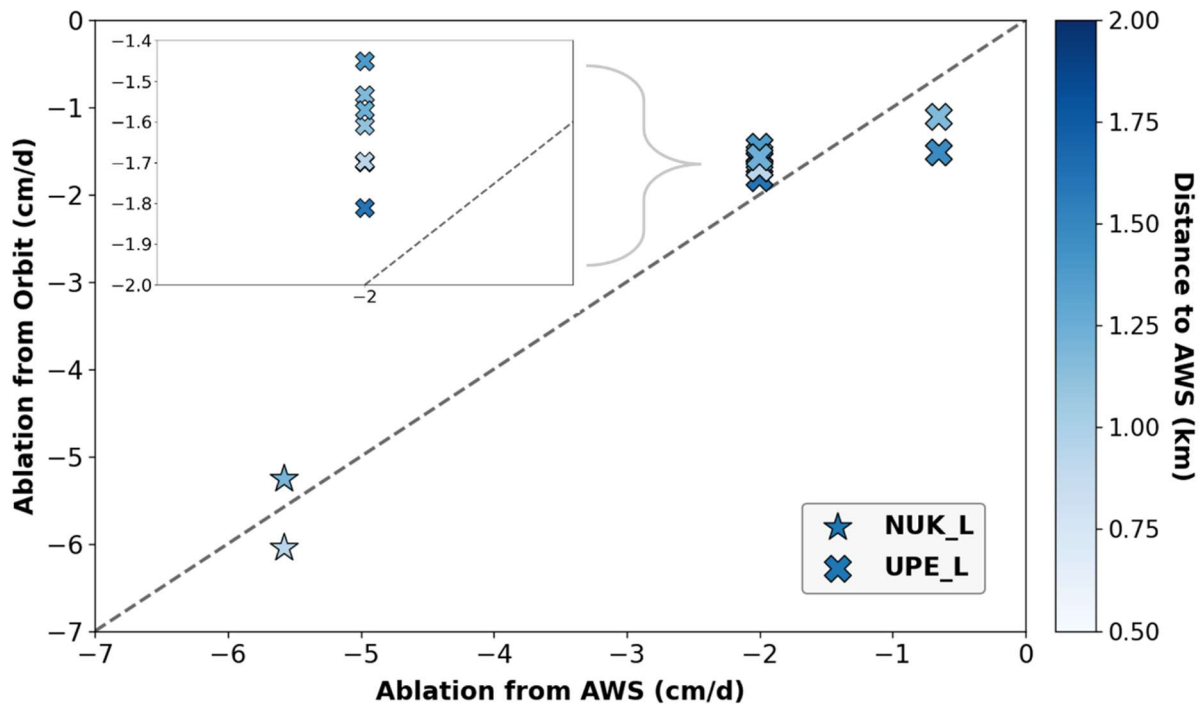


Figure 4.3: Comparison of mass continuity ablation rates to observed AWS ablation rates. The shapes indicate which AWS the measurement is compared to, and the shape color is the distance from the measurement to the AWS. The grey dotted line is a 1:1 line, representing equal mass continuity and AWS ablation rates. Ablation uncertainties are not included due to visual overlaps that are difficult to distinguish; still, all uncertainties encompass the 1:1 line, meaning observed AWS rates are plausible.

Thus, the mass continuity method is capable of closely reproducing observed rates near the AWS, across variable timescales, and at different outlet regions. Currently, SMB models particularly struggle to reproduce increasingly negative mass loss observations, as the models systematically underestimate observations greater than 2 m.w.e. (Fettweis et al., 2020). The mass continuity method shows a marked improvement, particularly for the -5.58 cm/d observed rate at NUK_L, which is the largest observed ablation rate in this study. The two mass continuity rates accurately describe this NUK_L observation within ± 0.48 cm/d, revealing that the mass continuity method can produce reliable rates when and where ablation is greatest. Being confident in the trend is difficult due to the limited sample size, however, this validation analysis provides evidence that our mass continuity method is robust, as ablation rates compare favorably to AWS observations, spatially and temporally. Including future AWS observations with new mass continuity rates, and expanding this study to other locations could yield unrepresented rates (-2.5 to -5 cm/d), which may strengthen these encouraging results.

5. Discussion

At UI and KNS, our mass continuity method demonstrates several common strengths. Expanding the scope of this study is needed for greater confidence, but mass continuity showed an ability to capture annual ablation changes, intra-annual variability, and spatial ablation gradients. Enhanced ablation in 2019 and the comparatively moderate rates of 2020 and 2021 are represented in our estimates. Similarly, we can quantify small and large observed seasonal ablation changes appropriately. These temporal capabilities have great potential to better understand the evolution of marginal GrIS SMB changes during temperate months, when mass losses are greatest, and to inform or calibrate RCM/SMB models in the low-lying ablation zone.

Our ablation estimates also describe coherent ablation gradients at incredibly high resolutions (2-5 km), and may reveal the spatial behavior of surface processes and difference in surface conditions. For example, local ablation gradients may be explained by existing surface melt channels, surface slope and aspect, surface albedo, wind speed, and prevailing wind direction. Perhaps, greater ablation rates are caused by enhanced surface melt via runoff channels, increased incident solar radiation based on surface aspect and albedo, and wind scour or snow redistribution depending on wind direction and surface slope. Similarly, wind speed, wind direction, and surface slope are important conditions for turbulent heat transfer during the summer, which is a major driver of melt in the lower ablation zone (van den Broeke et al., 2011), possibly explaining small-scale ablation gradients. Further, positive and balanced rates at UI and KNS may indicate ablation offset driven by avalanching or wind-blown snow from nearby mountains; nearly all of these rates are located close to mountainous topography. However, differentiating the causality of ablation gradients is complicated without detailed field observations. On regional scales, particularly at KNS, ablation magnitudes decline further inland, which is supported by the AWS observations. UI is more complex, as the region contains fewer outcrops or mountainous features, and the four marine-terminating glaciers likely affect the slow-flowing ice more freely. Also at UI, ablation magnitudes are generally larger near or on the fast-flowing glacier trunks, revealing one of the mass continuity method's limitations. Still, the method is able to identify not only temporal ablation changes, but also spatial changes, both of which are deficiencies in the marginal performance of current RCM/SMB models (Fettweis et al., 2020; Vernon et al., 2013).

While the mass continuity method has clear strengths, weaknesses also exist, particularly the unreasonable ablation rates on fast-flowing ice, the underestimation of observed rates at KNS, and the ablation rate uncertainties in general. The physical mechanisms responsible for large ablation estimates and uncertainties on fast-flowing ice are unclear, but we suggest a couple explanations.

First, some surface meltwater from slower-flowing areas is likely routed to the glacier trunks, where it ultimately pools or drains to the glacier bed. Meltwater pools that collect within the crevassed ice may ablate below the glacier surface, causing surface lowering and increased ablation. However, this process would be incredibly difficult to account for, and the more likely explanation lies within the crevassed ice itself. The ICESat-2 ATL06 product measures surface elevation changes, and by nature of fast flow, the 20 m resolution measurements are most definitely capturing different phases of the crevassed ice every 91 days. These highly variable surface measurements lead to extremely positive or negative ablation estimates, depending on the position of crevasses when the surface was measured. Therefore, we think ablation estimates on fast-flowing ice are not viable, limiting our method to only slow-flowing areas. Supporting this conclusion, the circle grid for the June to September 2020 ICESat-2 period at UI is largely located over faster-flowing ice and only returned two ablation rates; both rates are much greater than the AWS observations and have relatively large uncertainties.

At KNS, we underestimate the observed ablation during the two ICESat-2 periods of heightened ablation. While ablation has greater spatial variability at KNS and might explain some of the underestimation, the trend remains slightly concerning. After masking the positive (mass gain) ablation estimates, the average ablation for the May to August 2019 period changes from -2.97 cm/d to -3.26 cm/d, however, this new estimate still slightly underestimates the NUK_U observed rate (-3.31 cm/d); the July to September 2020 period does not have positive estimates and cannot be corrected. Fortunately, all 16 ablation estimates of the 2020 period are located further inland of the NUK_U station and closely resemble the physical conditions at NUK_U. Therefore, the average -1.77 cm/d rate is spatially consistent with the observed -1.83 cm/d rate. After masking positive estimates for the 2019 period, 101 ablation estimates remained. Approximately 65 of these 101 are located 35-55 km south of both KNS AWS stations; while not particularly close, the ~65 estimates are at surface elevations more analogous with the NUK_U station, therefore, the lower average ablation rate is justified. Although the 2019 and 2020 underestimations are explained by their relationships to NUK_U, assessing ablation rates far from an AWS is challenging without field observations.

At both sites, uncertainties are temporally consistent across the ICESat-2 periods, and although all estimates have an uncertainty less than ± 5 cm/d, the average uncertainties have similar magnitudes: ± 3.25 cm/d at KNS and ± 3.59 cm/d at UI. This suggests uncertainties are not only systematic over time, but also along the west-central coast of the GrIS, and possibly across the GrIS ablation zone with further testing. Still, we only report a small subset of ablation estimates from the circle grids (*Figure 3.1a*), as the majority of uncertainties are greater than ± 5 cm/d. While many of

these larger uncertainties are on fast-flowing ice and impacted by the ICESat-2 crevasse issue, our method would benefit if the uncertainties could be reduced and more ablation rates could be reported. Therefore, we focus on uncertainty analysis and identifying potential routes for improvement.

To better understand what controls the uncertainties, we calculate sensitivity coefficients for all terms in the ablation uncertainty equation (see *eq. 7*). Sensitivity coefficients reveal how equation terms are related to the equation's result. If a term is particularly sensitive (i.e. large coefficient), the term has greater potential to change the equation result, or in this case, the ablation uncertainty. For a consistent process, all 396 UI and KNS values for a single term are scaled by 10%, then we calculate new uncertainty values. The difference between the new uncertainty and original uncertainty, divided by the difference between the new and original term value is the sensitivity coefficient. Because the sensitivity coefficient magnitudes are similar at UI and KNS, we combine the sites and report a 396 coefficient average for all uncertainty terms (*Figure 5.1*), finding that velocity gradients, particularly error gradients, are the most sensitive terms. The thickness change rate error is also considerably sensitive, while all other terms have relatively low sensitivity.

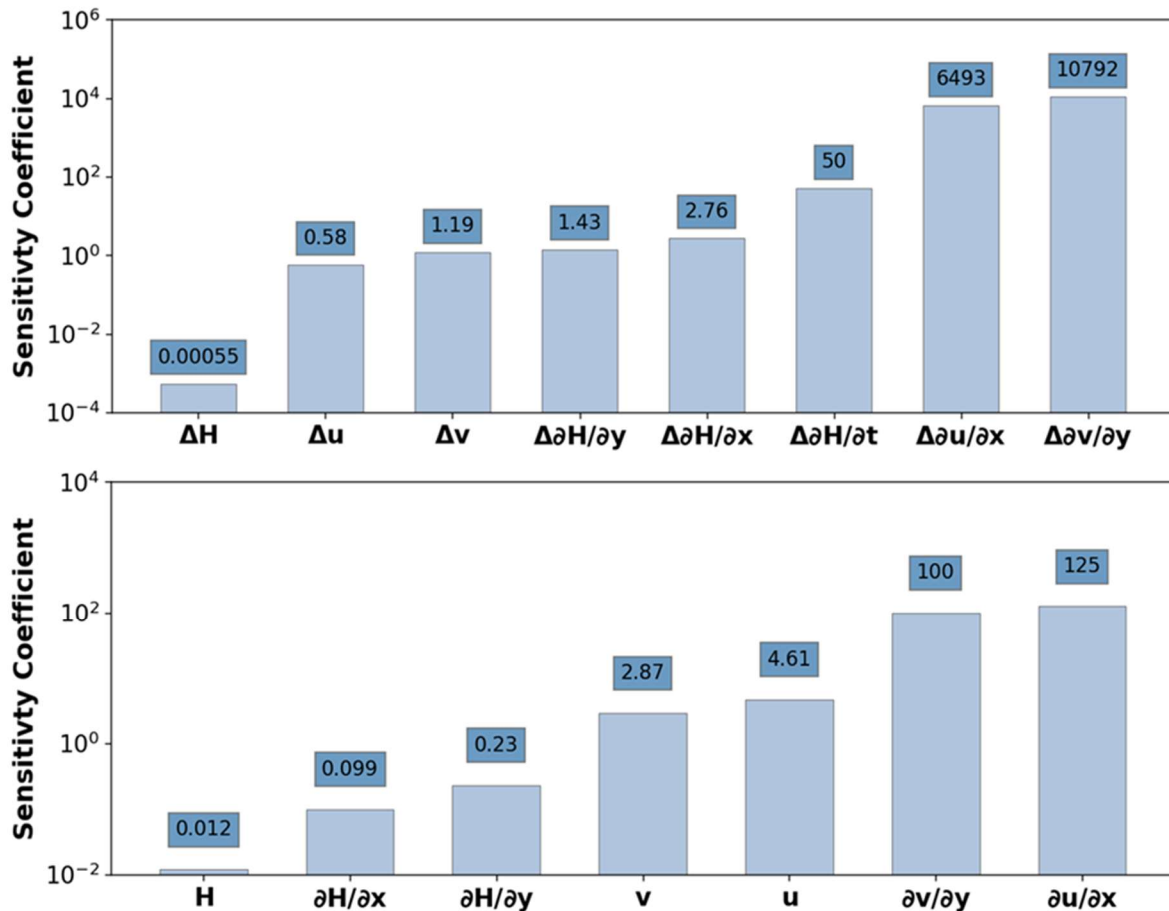


Figure 5.1: Sensitivity coefficients averaged for all 396 uncertainty estimates at UI and KNS. A coefficient is provided for each term in the ablation uncertainty equation. The top panel contains all error terms, and the bottom panel contains all measured terms. The coefficient values are inside the dark blue box.

While the sensitivity coefficients suggest that uncertainty changes should be dominated by velocity gradients, the observed uncertainty change somewhat disagrees. In addition to the sensitivity coefficients, we calculate the actual average uncertainty change when scaling each term by 10% and holding the others constant (*Figure 5.2*). On average, the scaled velocity gradients and thickness change rate errors increased the ablation uncertainty by ~ 0.05 - 0.13 cm/d, however, scaling the ice thickness resulted in the greatest change: ~ 0.17 cm/d. It is unclear why some terms ($\frac{\partial u}{\partial x}, \frac{\partial v}{\partial y}$) are characterized as sensitive, but do not exhibit much change, and conversely, why other terms ($H, u, \Delta \frac{\partial H}{\partial x}$, etc.) are not sensitive, but result in significant uncertainty changes. A plausible explanation might be that equation terms are more susceptible to change the uncertainty depending on the location of an estimate and the relative magnitudes of the terms themselves. Perhaps, the average term magnitude favors ice thickness as a facilitator of uncertainty change on slow-flowing ice.

Velocity gradients, in turn, may dominant uncertainty change on faster-flowing ice, where ice is likely to be more stressed and their magnitudes are larger.

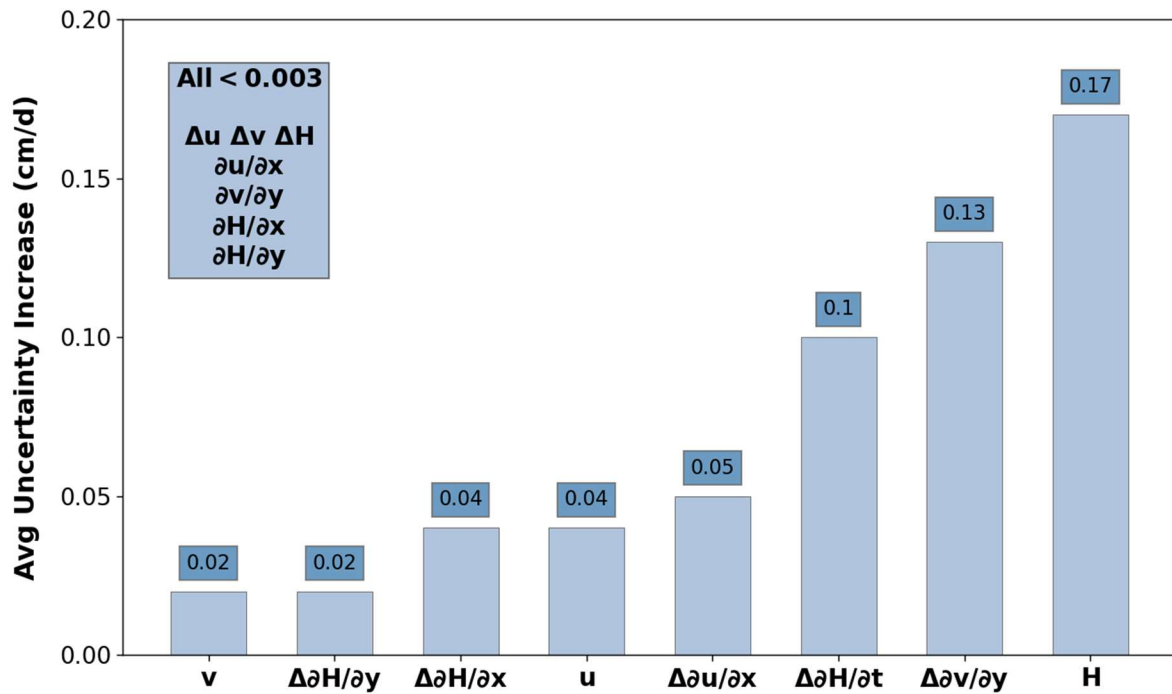


Figure 5.2: Average increase (cm/d) in the reported uncertainty after individually scaling each uncertainty term by 10% and keeping all other terms constant per iteration. The uncertainty change is averaged for all 396 estimates at UI and KNS. Average uncertainty changes are inside the dark blue boxes. The terms in the top-left box changed the uncertainty by less than 0.003 cm/d.

Despite an ambiguous relationship between term sensitivity and observed uncertainty change, we describe ideal conditions for producing low uncertainties with the mass continuity method. Of the 396 total estimates, 49 have uncertainties less than ± 2 cm/d, 205 are between ± 2 -4 cm/d, and 142 are between ± 4 -5 cm/d. Average term values are compared between these low, moderate, and high uncertainty sets (*Table 5.1*). The measured and error vector velocity ($u, v, \Delta u, \Delta v$) and ice thickness ($H, \Delta H$) terms, as well as the thickness change rate error ($\Delta \frac{\partial H}{\partial t}$), all have greater magnitudes in the high uncertainty set. Thickness gradient measurements and errors ($\frac{\partial H}{\partial x}, \frac{\partial H}{\partial y}, \Delta \frac{\partial H}{\partial x}, \Delta \frac{\partial H}{\partial y}$) are generally similar, but still slightly larger in the high uncertainty set. In addition, the high uncertainties have greater velocity gradient ($\frac{\partial u}{\partial x}, \frac{\partial v}{\partial y}$) magnitudes; however, the velocity gradient errors ($\Delta \frac{\partial u}{\partial x}, \Delta \frac{\partial v}{\partial y}$) are larger for the low uncertainty set. These findings further support that larger uncertainties are commonly located on faster-flowing, more dynamic ice. In general, the mass continuity method performs best over slow-flowing, low-stress areas, and there are opportunities to improve the uncertainties across faster-flowing areas.

Term (Units)	Low ($U < \pm 2$ cm/d)	Moderate ($\pm 2 < U < \pm 4$ cm/d)	High ($U > \pm 4$ cm/d)
$\Delta \frac{\partial H}{\partial t}$ (cm/d)	0.96	1.58	1.84
u (cm/d)	-1.81	-2.87	-6.91
Δu (cm/d)	1.79	1.91	2.12
v (cm/d)	1.88	1.84	4.08
Δv (cm/d)	2.48	2.71	2.74
$\frac{\partial u}{\partial x}$ (1/d)	-9.6E-06	-1.1E-05	-2.2E-05
$\Delta \frac{\partial u}{\partial x}$ (1/d)	1.0E-04	9.2E-05	8.7E-05
$\frac{\partial v}{\partial y}$ (1/d)	-4.0E-06	2.2E-06	1.7E-05
$\Delta \frac{\partial v}{\partial y}$ (1/d)	1.6E-04	1.7E-04	1.5E-04
$\frac{\partial H}{\partial x}$ *	0.049	0.048	0.036
$\Delta \frac{\partial H}{\partial x}$ *	0.141	0.158	0.168
$\frac{\partial H}{\partial y}$ *	-0.014	0.023	0.029
$\Delta \frac{\partial H}{\partial y}$ *	0.141	0.159	0.171
H (m)	68	147	248
ΔH (m)	30	33	35

Table 5.1: Average term value for low, moderate, and high uncertainty classifications, combined at UI and KNS. Asterisks indicate unitless terms.

While we are confident in the mass continuity method as currently constructed, potential method adjustments may make the ablation rates more precise and reduce the uncertainties. Quick modifications that could be beneficial include a different velocity smoothing function or kernel size,

dynamic ablation circle diameters, and larger spatially averaged ATL06 thickness change points (i.e. > 40 m). Ablation rates could also be estimated at a 150 m resolution, on a cell-by-cell basis, which may prove to be a more powerful tool. One major idea that could considerably improve the 91-day median velocity measurements and the mean sampled difference metric is developing a historically referenced periodicity of velocity, which might capture seasonal velocity fluctuations more adequately than daily, linear interpolation through a handful of sampled dates. By collecting velocity observations, at a given study site, over the past 10-20 years, perhaps a smoothing function can capture typical, temporal velocity variations. Improving the velocity time-series would certainly result in more precise ablation rates; likewise, the mean sampled difference, which accounts for time-interpolation in the velocity error, would benefit from a smoothed historical time-series that might reduce ablation uncertainty. Just like the mean sampled difference, the effect of all operations performed on measured terms are accounted for in the respective errors, with conservative thresholds. More aggressive methods and thresholds, such as a tighter thickness change rate prediction interval, smaller infilling error velocities, expanded reconstruction censoring, velocity-specific reconstruction errors, and a more skilled temporal interpolation metric would surely alter the uncertainties, but the effects are currently unclear. Another effort could involve using more AWS variables, such as temperature and snow surface data, to be truly confident in the observed ablation time series. The AWS data is indeed from the field, particularly the harsh ablation zone, making the time-series messy and difficult to interpret. There are many possibilities to improve this mass continuity method, however, further testing is needed, and balancing being too aggressive, conservative, and subjective with future decisions is important.

Moving forward, three major opportunities are presented to expand on this study, all of which have incredible potential to further improve our understanding of ablation rates around the GrIS margins. First, future mass continuity ablation estimates could be validated with field observations, using the glaciological method (Cuffey and Paterson, 2010). Drilling ablation stakes into the ice, then measuring the ice surface before and after the summer would provide field validated ablation rates. One advantage of this method is the ability to select multiple installation sites across a glacier outlet region not near AWSs. In this way, more observations are located throughout the region, which would help validate ablation estimates far from the AWSs. Because reasonable uncertainties are important, circle selection should be optimized based on where past estimate uncertainties were consistently low (i.e. areas/circles with multiple estimates). Another potential difficulty is the data return of ICESat-2; if the satellite passes over on a cloudy/foggy day, then the surface elevation measurements may be spotty or missing entirely. Still, more dispersed field validated observations would help establish greater spatial confidence in the mass continuity method presented here,

especially for non-validated estimates not near AWSs. Second, if spatial confidence is established to where AWS observations are not necessary, the mass continuity method may be scaled across much of the GrIS margin, within the extent of other MEaSUREs velocity grids. The MEaSUREs dataset has 55 total velocity grids, predominantly located on Greenland's north, west, and southeast coasts. While some of the grids have been discontinued, there is potential to apply this method at many other glacier outlet regions from 2019 until the ICESat-2 or MEaSUREs missions are terminated. In this study, UI and KNS were selected due to their exceptional spatial and temporal satellite coverage, and more importantly, because both sites had two PROMICE AWSs, facilitating validation. Without the restraints of needing AWS validated estimates, the mass continuity method may be implemented wherever MEaSUREs and ICESat-2 observations exist. Third, our ablation rates at UI and KNS, or future regions, may be compared to the marginal outputs of RCM/SMB models such as RACMO, MAR, and HIRHAM. Such an effort might help inform and improve these models spatial and temporal deficiencies around the GrIS margin.

6. Conclusions

The mass continuity method presented here, provides a new mass budget-based approach for quantifying ablation rates at high resolutions, in the GrIS ablation zone. New and powerful satellite datasets including ICESat-2, IceBridge BedMachine, and MEaSURES enable such ablation measurements through the 2-D mass continuity equation. We directly calculate ablation rates during warmer months, on seasonal timescales, by combining temporal ice thickness change observations with thickness changes caused by dynamic flow. The results indicate slow-flowing and low-stress ice typically produces the most precise ablation rates and lowest uncertainties. AWS observations facilitate ablation validation, and we find that our ablation rates largely agree with observed rates, especially for estimates located near or at similar physical conditions as the AWS. Validating more ablation rates closely positioned to an AWS will certainly improve spatial confidence in estimates not near the AWS. This is a crucial step for potentially implementing the mass continuity method across more of the GrIS margin.

This study was developed to complement recent mass balance and SMB model intercomparison projects (Fettweis et al., 2020; Hanna et al., 2020; Vernon et al., 2013), and to act on recommendations of using satellite data and in-situ observations to reconcile spatial and temporal ablation rates near the ice sheet margin. RCM/SMB model performance would benefit from more measurements that better represent the physical processes controlling mass loss, and our method is able to partition dynamic thickness and ice surface changes at regions with scarce field observations. Improving marginal model performance is critical for future surface mass loss and sea level rise projections. We believe the mass continuity method is a robust tool for properly representing spatial and temporal mass loss gradients. Still, future efforts need to focus on reducing uncertainties, validating more ablation rates with AWS observations, manual field validation, and comparing ablation rates with RCM/SMB outputs.

7. References

- Andrews, L. C., Catania, G. A., Hoffman, M. J., Gulley, J. D., Luthi, M. P., Ryser, C., et al. (2014). Direct observations of evolving subglacial drainage beneath the Greenland Ice Sheet. *Nature*, *514*(7520), 80–83. <https://doi.org/10.1038/nature13796>
- Catania, G.A., Stearns, L.A., Moon, T., Enderlin, E., & Jackson, R.H. (2020). Future evolution of greenland's marine-terminating outlet glaciers. *Journal of Geophysical Research: Earth Surface*, *125*, e2018JF004873. <https://doi.org/10.1029/2018JF004873>
- Cuffey, K. M., & Paterson, W. S. B. (2010). Physics of glaciers, *Fourth Edition. The Physics of Glaciers*.
- Enderlin, E. M., Howat, I. M., Jeong, S., Noh, M. J., Van Angelen, J. H., & Van Den Broeke, M. R. (2014). An improved mass budget for the Greenland Ice Sheet. *Geophysical Research Letters*, *41*, 866–872. <https://doi.org/10.1002/2013GL059010>
- Ettema, J., van den Broeke, M. R., van Meijgaard, E., van de Berg, W. J., Box, J. E., & Steffen, K. (2010). Climate of the Greenland ice sheet using a high-resolution climate model –Part 1: Evaluation. *The Cryosphere*, *4*, 511–527, <https://doi.org/10.5194/tc-4-511-2010>
- Fausto, R. S., van As, D., Mankoff, K. D., Vandecrux, B., Citterio, M., Ahlstrøm, A. P., et al. (2021). Programme for Monitoring of the Greenland Ice Sheet (PROMICE) automatic weather station data. *Earth System Science Data*, *13*, 3819–3845. <https://doi.org/10.5194/essd-13-3819-2021>
- Fettweis, X., Hofer, S., Krebs-Kanzow, U., Amory, C., Aoki, T., Berends, C. J., et al. (2020). GrSMBMIP: Intercomparison of the modelled 1980–2012 surface mass balance over the Greenland Ice Sheet. *The Cryosphere*, *14*(11), 3935–3958. <https://doi.org/10.5194/tc-14-3935-2020>
- Hanna, E., Huybrechts, P., Janssens, I., Cappelen, J., Steffen, K., & Stephens, A. (2005). Runoff and mass balance of the Greenland ice sheet: 1958–2003. *Journal of Geophysical Research: Atmospheres*, *110*, D13108. <https://doi.org/10.1029/2004JD005641>
- Hanna, E., Pattyn, F., Navarro, F., Favier, V., Goelzer, H., van den Broeke, M. R., et al. (2020). Mass balance of the ice sheets and glaciers—Progress since AR5 and challenges. *Earth-Science Reviews*, *201*, 102976. <https://doi.org/10.1016/j.earscirev.2019.102976>

- Howat, I. M., Negrete, A., & Smith, B. E. (2014). The Greenland Ice Mapping Project (GIMP) land classification and surface elevation datasets. *The Cryosphere*, 8(4), 1509–1518.
<https://doi.org/10.5194/tc-8-1509-2014>
- IPCC. (2014). Climate Change 2014: Synthesis Report. Contribution of Working Groups I, II and III to the Fifth Assessment Report of the Intergovernmental Panel on Climate Change [Core Writing Team, R.K. Pachauri and L.A. Meyer (eds.)]. IPCC, Geneva, Switzerland, 151 pp.
- Joughin, I. (2002). Ice-sheet velocity mapping: a combined interferometric and speckle-tracking approach. *Annals of Glaciology*, 34, 195–201. <https://doi.org/10.3189/172756402781817978>
- Joughin, I., Smith, B. E., Howat, I. M., Scambos, T., & Moon, T. (2010). Greenland flow variability from ice-sheet-wide velocity mapping. *Journal of Glaciology*, 56(197), 415–430.
<https://doi.org/10.3189/002214310792447734>
- Karlsson, N. B., Solgaard, A. M., Mankoff, K. D., Gillet-Chaulet, F., MacGregor, J. A., Box, J. E., et al. (2021). A first constraint on basal melt-water production of the Greenland ice sheet. *Nature Communications*, 12, 3461. <https://doi.org/10.1038/s41467-021-23739-z>
- Larsen, S. H., Khan, S. A., Ahlstrøm, A. P., Hvidberg, C. S., Willis, M. J., & Andersen, S. B. (2016). Increased mass loss and asynchronous behavior of marine-terminating outlet glaciers at Upernavik Isstrøm, NW Greenland. *Journal of Geophysical Research: Earth Surface*, 121, 241–256. <https://doi.org/10.1002/2015JF003507>
- Markus, T., Neumann, T., Martino, A., Abdalati, W., Brunt, K., Csatho, B., et al. (2017). The Ice, Cloud, and land Elevation Satellite-2 (ICESat-2): Science requirements, concept, and implementation. *Remote Sensing of Environment*, 190, 260–273.
<https://doi.org/10.1016/j.rse.2016.12.029>
- Morlighem, M., Rignot, E., Mouginot, J., Seroussi, H., & Larour, E. (2014b). High-resolution ice thickness mapping in south Greenland. *Annals of Glaciology*, 55(67), 64–70.
<https://doi.org/10.3189/2014AoG67A088>
- Morlighem, M., Rignot E., Mouginot J., Wu X., Seroussi H., Larour E., & Paden, J. (2013). High-resolution bed topography mapping of Russell Glacier, Greenland, inferred from Operation IceBridge data. *Journal of Glaciology*, 59(218):1015–1023.
<https://doi.org/10.3189/2013JoG12J235>

- Morlighem, M., Williams, C. N., Rignot, E., An, L., Arndt, J. E., Bamber, J. L., et al. (2017). BedMachine v3: Complete bed topography and ocean bathymetry mapping of Greenland from multibeam echo sounding combined with mass conservation. *Geophysical Research Letters*, *44*, 11,051–11,061. <https://doi.org/10.1002/2017GL074954>
- Motyka, R. J., Cassotto, R., Truffer, M., Kjeldsen, K. K., Van As, D., Korsgaard, N. J., et al. (2017). Asynchronous behavior of outlet glaciers feeding Godthåbsfjord (Nuup Kangerlua) and the triggering of Narsap Sermia's retreat in SW Greenland. *Journal of Glaciology*, *63*(238), 288–308. <https://doi.org/10.1017/jog.2016.138>
- Mouginot, J., Rignot, E. J., Bjørk, A. A., van den Broeke, M. R., Millan, R., Morlighem, M., et al. (2019). Forty-six years of Greenland Ice Sheet mass balance from 1972 to 2018. *Proceedings of the National Academy of Sciences*, *116*(19), 9239–9244. <https://doi.org/10.7280/D1MM37>
- Moyer, A. N., Nienow, P. W., Gourmelen, N., Sole, A. J., & Slater, D. A. (2017). Estimating spring terminus submarine melt rates at a Greenlandic tidewater glacier using satellite imagery. *Frontiers in Earth Science*, *5*, 107. <https://doi.org/10.3389/feart.2017.00107>
- Noël, B., van de Berg, W. J., Machguth, H., Lhermitte, S., Howat, I., Fettweis, X., & van den Broeke, M. R. (2016). A daily, 1 km resolution data set of downscaled Greenland ice sheet surface mass balance (1958–2015). *The Cryosphere*, *10*, 2361–2377. <https://doi.org/10.5194/tc-10-2361-2016>
- Noël, B., van de Berg, W. J., van Wessem, J. M., van Meijgaard, E., van As, D., Lenaerts, J. T. M., et al. (2018). Modelling the climate and surface mass balance of polar ice sheets using RACMO2—Part 1: Greenland (1958–2016). *The Cryosphere*, *12*(3), 811–831. <https://doi.org/10.5194/tc-12-811-2018>
- Rignot, E., Box, J. E., Burgess, E., & Hanna, E. (2008). Mass balance of the Greenland ice sheet from 1958 to 2007. *Geophysical Research Letters*, *35*, L20502. <https://doi.org/10.1029/2008gl035417>
- Rignot, E. J., & Kanagaratnam, P. (2006). Changes in the velocity structure of the Greenland Ice Sheet. *Science*, *311*, 986–990. <https://doi.org/10.1126/science.1121381>
- Rietbroek, R., Brunnabend, S. E., Kusch, J., Schröter, J., and Dahle, C. (2016). Revisiting the contemporary sea-level budget on global and regional scales. *Proceedings of the National Academy of Sciences*, *113*, 1504–1509. <https://doi.org/10.1073/pnas.1519132113>

- Shepherd, A., Ivins, E. R., Geruo, A., Barletta, V. R., Bentley, M. J., Bettadpur, S., et al. (2012). A reconciled estimate of ice-sheet mass balance. *Science*, 338(6111), 1183–1189. <https://doi.org/10.1126/science.1228102>
- Smith, B., Fricker, H., Gardner, A., Medley, B., Nilsson, J., Paolo, F., et al. (2020). Pervasive ice sheet mass loss driven by competing ocean and atmosphere processes. *Science*, 368(6496), 1239–1242. <https://doi.org/10.1126/science.aaz5845>
- Smith, B., Fricker, H., Holschuh, N., Gardner, A., Adusumilli, S., Brunt, K., et al. (2019). Land ice height-retrieval algorithms for NASA's ICESat-2 photon-counting laser altimeter. *Remote Sensing of Environment*, 233, 111352. <https://doi.org/10.1016/j.rse.2019.111352>
- The IMBIE Team. (2020). Mass balance of the Greenland Ice Sheet from 1992 to 2018. *Nature*, 579, 233–239. <https://doi.org/10.1038/s41586-019-1855-2>
- Van As, D., Andersen, M. L., Petersen, D., Fettweis, X., Van Angelen, J. H., Lenaerts, J. T. M., et al. (2014). Increasing meltwater discharge from the Nuuk region of the Greenland ice sheet and implications for mass balance (1960–2012). *Journal of Glaciology*, 60(220), 314–322. <https://doi.org/10.3189/2014JoG13J065>
- van den Broeke, M., Bamber, J., Ettema, J., Rignot, E., Schrama, E., van de Berg, W. J., van Meijgaard, E., Velicogna, I., & Wouters, B. (2009). Partitioning Recent Greenland Mass Loss. *Science*, 326, 984–986. <https://doi.org/10.1126/science.1178176>
- van den Broeke, M. R., Enderlin, E. M., Howat, I. M., Munneke, P. K., Noël, B. P. Y., van de Berg, W. J., et al. (2016). On the recent contribution of the Greenland ice sheet to sea level change. *The Cryosphere*, 10, 1933–1946. <https://doi.org/10.5194/tc-10-1933-2016>
- van den Broeke, M. R., Smeets, C. J. P. P., Van De Wal, R. S. W. (2011). The seasonal cycle and interannual variability of surface energy balance and melt in the ablation zone of the west Greenland ice sheet. *The Cryosphere*, 5(2), 377–390. <https://doi.org/10.5194/tc-5-377-2011>
- Vernon, C. L., Bamber, J. L., Box, J. E., van den Broeke, M. R., Fettweis, X., Hanna, E., Huybrechts, P. (2013). Surface mass balance model intercomparison for the Greenland ice sheet. *The Cryosphere*, 7, 599–614. <https://doi.org/10.5194/tc-7-599-2013>